Research Square

Preprints are preliminary reports that have not undergone peer review.
They should not be considered conclusive, used to inform clinical practice,
or referenced by the media as validated information.

Parametric Sensitivity Assessment of Slip Flow and Thermophoretic Effects on a Vertical Stretching Surface Using Response Surface Methodology

S Ramesh

Vellore Institute of Technology University

H Niranjan

niranjan.hari@vit.ac.in

Vellore Institute of Technology University

Article

Keywords: ANN, RSM, Sensitivity analysis, Slip velocity, Energy slip, Thermophoresis parameter

Posted Date: July 2nd, 2026

DOI: https://doi.org/10.21203/rs.3.rs-10016277/v1

License: This work is licensed under a Creative Commons Attribution 4.0 International License.
Read Full License

Additional Declarations: No competing interests reported.

Version of Record: A version of this preprint was published at Scientific Reports on November 2nd, 2026.
See the published version at https://doi.org/10.1038/s41598-026-77054-y.

Parametric Sensitivity Assessment of Slip Flow and Thermophoretic Effects on a Vertical Stretching Surface Using Response Surface Methodology

S Ramesh, H Niranjan*
Vellore Institute of Technology, Vellore, India.
ramesh.s2023@vitstudent.ac.in, niranjan.hari@vit.ac.in*

Abstract

This study investigates the effect of velocity slip on magnetohydrodynamic boundary-layer flow, emphasizing energy slip and thermophoresis under steady-flow conditions. While Magnetic Resonance Imaging (MRI) employs specialized equipment to generate detailed internal images through proton alignment, the present work focuses on fluid-dynamic mechanisms governing heat and mass transfer. The governing partial differential equations are transformed into ordinary differential equations using similarity transformations and solved with MATLAB's bvp4c solver. A sensitivity analysis is performed to optimize heat transfer performance, representing a key novelty of the study. The results reveal that increasing the velocity slip parameter from 0.7 to 1.9 significantly alters the velocity and temperature profiles, leading to an enhancement of the Nusselt number by approximately 3.3% and a reduction in skin friction by nearly 19.3%. The influence of the dipole effect on flow characteristics is also examined. Furthermore, Artificial Neural Networks (ANN) demonstrate superior predictive accuracy compared to Response Surface Methodology (RSM). Comparison with earlier studies confirms the validity of the results. Overall, the findings demonstrate the potential of velocity slip to enhance heat transfer more effectively than energy slip and thermophoresis in advanced thermal management systems.

Keywords: ANN, RSM, Sensitivity analysis, Slip velocity, Energy slip, Thermophoresis parameter.

Nomenclature

λ- Thermal conductivity
Nr - Buoyancy ratio parameter
β- Volumetric expansion parameter
α_1- Reciprocal of the magnetic Prandtl number
Nb- Brownian diffusion parameter
Pr - Prandtl number of base fluids
σ- Dimensionless reaction rate
Nc - Regular buoyancy parameter
δ- Temperature difference parameter
n- Fitted rate constant
E- non-dimensional activation energy
L_1- Velocity slip parameter
L_2 - Energy slip parameter
Nt - Thermophoresis parameter
Ec - Eckert number
Rd - Thermal radiation parameter
Df- Dufour number
Sc- Schmidt number
Sr- Soret parameter
f' - Velocity profile
g' - Dimensionless magnetic induction components
θ - Temperature profile
φ - Concentration profile
χ - Solute concentration profile

1. Introduction

Velocity slip occurs when the fluid velocity at a solid boundary differs from the velocity of the surface. This phenomenon arises due to microscale effects, fluid rarefaction, or the presence of surface coatings, allowing the fluid to move relative to the wall instead of adhering completely to it. This phenomenon is significantly depended on all three types of flow systems microfluidic, nanofluid and EMHD. In previous research, the effects of Brownian motion and thermophoresis on the temperature field were improved and the concentration of nanoparticles was reduced for the MHD Williamson nanofluid flow in a microchannel with slip and convective boundary conditions. Graphical analysis was also utilized to study the effect of heat flux on wall drag [1]. The heat transfer characteristics of fluid flow over a convectively heated stretching surface in the presence of a magnetic field shows that surface convection, magnetic effects and viscous dissipation all contribute to increased temperature distribution while velocity slip reduces it [2]. The velocity field is decreased with increasing the nanoparticle volume fraction and slip parameters in the three-dimensional EMHD flow of ZnO-water nanofluid over a bidirectional Riga plate, whereas the temperature profile is increased with increasing the solid volume fraction and thermal Biot numbers [3]. Magnetic field strength, slip and suction in surface drag and heat transfer promote MHD nanofluid flow across a permeable stretched sheet contained in a porous media while viscous dissipation thickens thermal boundary layer [4]. The investigations of nanofluid flow across nonlinear stretching sheets demonstrate that the impacts of the electric field are enhanced the velocity and temperature distributions [5] and the larger magnetic field retards the nanoparticle mobility. Many works have also been devoted to heat and mass transport in the presence of EMHD forces and slip situations. Apart from Nusselt and Sherwood numbers, the flow behavior is substantially affected by the modified Hartmann number, thermophoresis, Brownian motion and slip parameters [6]. Thermal and diffusion slip effects diminish the rate of heat and mass transfer in EMHD stagnation-point micropolar nanofluid flows. The parameters associated with buoyancy have a significant influence on the temperature and concentration fields [7]. In addition, the EMHD Carreau nanofluid slip flows have enhanced the rate of mass and heat transfer by changing the thermophysical and bioconvective parameters [8]. Moreover, the thermal performance of EMHD nanofluids has been explored for engineering and biomedical applications. Skin friction qualities of blood-gold nanofluids are significantly affected by the particle size and spacing; nonetheless, a rise in volume % of nanoparticles promotes heat transmission and minimizes drag [9]. Studies on hybrid nanofluids have shown the importance of mass diffusivity and variable thermal conductivity in maximizing energy consumption, heat transfer enhancement and entropy producing features [10]. Studies on electrokinetic microchannels have been gained further insight on roles of electric double layer effects, thermal radiation, viscous dissipation and Joule heating on heat transmission [11]. Recent research has tried to improve the understanding of transport processes by considering the effects of chemical reactions, solar radiation, activation energy and gyrotactic microorganisms. Entropy production studies on EMHD Jeffrey nanofluids with nanoparticles and microorganisms [12] revealed the role of viscous dissipation, Ohmic heating and internal heat sources. Thermophoresis, Brownian motion, magnetic inclination and slip effects are important elements affecting the fluid transport properties as presented in bioconvective hybrid nanofluid models [13]. Studies of maxwell nanofluids indicate that the thermophoresis and Brownian motion increase the temperature distributions, whilst the fluid elasticity decreases the velocity [14]. In the study of 3D doubly diffusive nanoliquid flow in Darcy-Forchheimer porous media, it is found that the activation energy plays a vital role on solutal transport while the inertial and rotational effects reduce heat transfer rates [15]. Hybrid nanofluid flow over a bidirectionally stretching sheet has been shown to enhance thermal distribution while reducing the velocity field. The hybrid mixture exhibits superior heat-transfer characteristics and lower surface drag compared with conventional nanofluids [16]. The influence of partial slip on electrically conducting micropolar fluid flow toward a shrinking sheet under a transverse magnetic field has also been investigated, revealing that the governing parameters significantly affect both flow and heat-transfer characteristics for assisting and opposing flows [17]. Magneto-micropolar electrically conducting nanofluid flow over a linearly stretching sheet subjected to convective heating, nonlinear thermal radiation, Joule heating, velocity slip, viscous dissipation, and mixed convection demonstrated that nonlinear thermal radiation markedly enhances the temperature field, while the electric field exerts a dominant influence over the magnetic field [18]. The flow of electrically conducting hybrid nanofluids over rotating bidirectional stretching surfaces containing gyrotactic microorganisms has further highlighted the importance of thermophoresis, Brownian motion, thermal radiation, heat generation, and chemical reactions in improving heat-transfer performance and supporting biomedical applications [19]. Bioconvective MHD flows of non-Newtonian fluids have shown that magnetic effects enhance velocity while suppressing

microorganism motility. Heat generation and thermal radiation increase the temperature field, whereas fluid rheology significantly influences transport characteristics [20]. The thermal and fluid-dynamic behavior of Williamson hybrid nanofluids has revealed that velocity decreases with increasing permeability and squeezing effects, while magnetic influences improve the velocity distribution. Heat-transfer rates are strengthened with increasing squeezing parameters [21]. The combined effects of buoyancy, Brownian motion, thermophoresis, activation energy, and chemical reactions have also been explored extensively. It has been reported that activation energy increases nanoparticle concentration, chemical reactions suppress heat transfer, and Brownian motion acts opposite to thermophoresis [22]. Investigations of radiative MHD flow over exponentially stretching surfaces have shown that magnetic effects increase momentum boundary-layer thickness, particularly under convective boundary conditions [23]. Furthermore, nonlinear thermal radiation and Arrhenius activation energy significantly influence heat-transfer characteristics in Casson and Maxwell fluids, with Casson fluids exhibiting higher average heat-transfer rates [24]. Recent studies on mixed-convective MHD stagnation-point flow have identified convection as a dominant factor governing transient flow behavior, although several important transport mechanisms remain unexplored [25]. Optimization analyses of nonlinear radiative hydromagnetic CNT hybrid nanofluids have demonstrated that both SWCNT and MWCNT nanoparticles reduce velocity while enhancing temperature, with the Hamilton–Crosser model providing superior heat-transfer performance compared with the Yamada–Ota model [26]. Advances in energy and fluid-transport systems have further shown that improved slip-vortex modelling enhances pump efficiency and prediction accuracy under variable-speed operating conditions [27]. The flow of Maxwell hybrid nanofluids in inclined and vertical cylinders under magnetic dipole effects has also been examined, where artificial neural network models accurately predicted skin-friction, Nusselt number, and Sherwood number characteristics [28]. A recent study [29] examined mixed convection of Casson nanofluids over an exponential stretching surface with induced magnetic fields, Hall currents, surface roughness, and chemical reactions. The results demonstrated strong sensitivity of the velocity, temperature, and concentration fields to the controlling parameters.

1.1 Novelty, scope and objectives

This study is the first to systematically and thoroughly investigate how the velocity slip parameter and energy slip parameter work together to affect the flow of the boundary layer over a vertical sheet, as well as how to improve thermal performance.

The research examines the impact of variations in velocity slip and energy slip parameters on the momentum, thermal, and concentration boundary-layer structures within a vertical sheet configuration.

To study how the flow, temperature, and concentration profiles along a vertical sheet are affected by the velocity slip and energy slip parameters, both on their own and together.

2. Mathematical formulation

Fig. 1 shows the two-dimensional boundary layer flow over a stretched sheet. The stretching of the sheet is continuous, which causes the formation of a boundary layer and the fluid motion near the sheet. The model investigates the impacts of thermophoresis, energy slip, and velocity slip on transport processes. The thermal and momentum boundary layers represent the distributions of temperature and momentum within the flow region. Furthermore, the solute and concentration boundary layers characterize the movement of nanoparticles and other species near the surface. The diagram depicts a two-dimensional laminar boundary-layer flow of an electrically conducting nanofluid across a vertically oriented stretching surface. The coordinate system is defined as follows: x measures distance down the sheet, y represents normal direction, with u and v representing velocity components in these directions. T and C represent the temperature and nanoparticle concentration fields, respectively, with free-stream values of $T\infty$ and $C\infty$. A uniform transverse velocity slip parameter of L_1 is applied, creating a Lorentz force that affects momentum transport in the magnetohydrodynamic (MHD) flow. The physical model is governed by coupled nonlinear partial differential equations for momentum conservation, thermal energy, and species concentration, each subject to appropriate surface conditions at $y = 0$ and asymptotic limits as $y \rightarrow \infty$. By incorporating appropriate similarity transformations, the governing PDEs are reduced to a system of ordinary differential equations that capture the effect of velocity slip parameter interaction, thermal gradients, diffusion mechanisms, and nanoparticle

dynamics on the resulting velocity, temperature, and concentration distributions along the vertical stretching sheet.

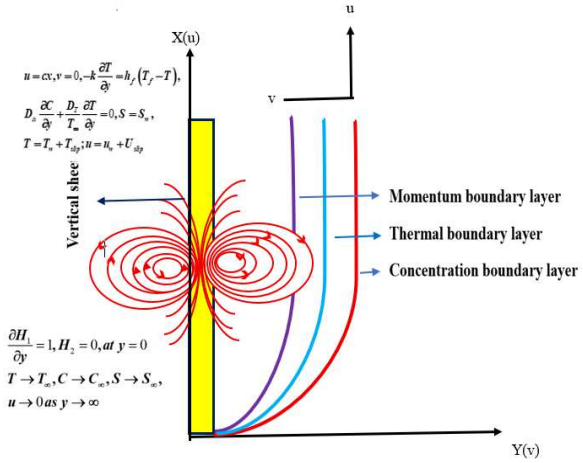


Fig. 1. Vertical Stretching Sheet Flow Geometry

2.1 Physical description and mathematical modeling

Fig. 2 shows how a nanofluid passing through a channel, where nanoparticles improve heat transfer from the heated surface, can cool an electronic device. Velocity slip L_1 energy slip L_2 impact the boundary layer's behavior, altering fluid motion and thermal interaction near the wall. Thermal radiation facilitates additional heat transfer from the heated area to the surrounding fluid. The interaction of radiative heat transfer, slip effects, and nanoparticle dispersion enhances the system's total cooling performance. Visualized in Fig. 3 is the computational process that was utilized to examine the transport phenomena within the suggested flow model. The MATLAB BVP4C solver is used to numerically solve the governing equations under the specified boundary conditions once they are translated into a dimensionless form. After processing the results, various physical parameters can be represented graphically and numerically. The results are then validated and subjected to sensitivity analysis using ANN and RSM, as well as compared to previous research, to guarantee their dependability.

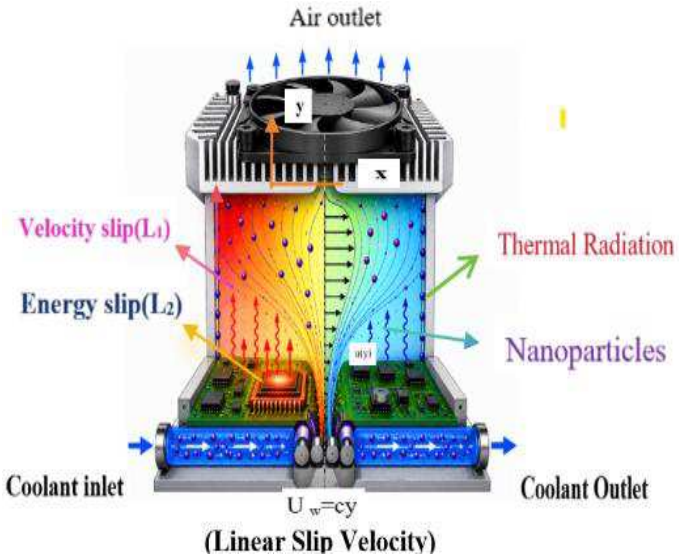


Fig. 2 Practical Applications of Nanofluids in Engineering.

2.2 Formulation of Governing Equations in Dimensional Terms

$$\frac{\partial u}{\partial x}+\frac{\partial v}{\partial y}=0 \tag{1}$$

$$\frac{\partial H_1}{\partial x}+\frac{\partial H_2}{\partial y}=0 \tag{2}$$

Equation (1) is the continuity equation that embodies the principle of mass conservation in the domain of fluid flow. It checks the flow field for imbalances and makes sure the net mass entering and leaving the control volume is balanced. The conservation of mass within the flow field is expressed by Equation (2), the continuity equation. It means that there is no divergence in the flow since the net rate of fluid entering and leaving the control volume is balanced.

$$u\frac{\partial u}{\partial x}+v\frac{\partial u}{\partial y}=v_f\frac{\partial^2 u}{\partial y^2}+\frac{1}{\rho_f}\left[\left(1-c_\infty\right)\rho f_\infty\beta\left(T-T_\infty\right)-\left(\rho_p-\rho_{f\infty}\right)\left(c-c_\infty\right)\right]g+\frac{\mu}{4\pi\rho_f}\left(H_1\frac{\partial H_1}{\partial x}+H_2\frac{\partial H_1}{\partial y}\right) \tag{3}$$

$$u\frac{\partial H_1}{\partial x}+v\frac{\partial H_2}{\partial y}=H_1\frac{\partial u}{\partial x}+H_2\frac{\partial u}{\partial y}+\mu_e\frac{\partial^2 H_1}{\partial y^2} \tag{4}$$

Equation (3) illustrates the conservation of momentum in the flow field by considering the effects of inertia, viscous diffusion, pressure gradients, and external body forces. It measures the velocity distribution of the boundary layer and defines the internal force balance of the fluid. As a result of both magnetic diffusion and fluid velocity, Equation (4) explains how the induced magnetic field moves through the fluid. The fundamental behavior of magnetohydrodynamic (MHD) flows is shown by the interaction between the flow field and the magnetic field.

$$u\frac{\partial T}{\partial x}+v\frac{\partial T}{\partial y}=-\frac{\alpha}{k}\frac{\partial q_r}{\partial y}+\alpha\frac{\partial^2 T}{\partial y^2}+\beta\,k_r^2\left(\frac{T}{T_\infty}\right)^n\exp\left(-\frac{E\alpha}{kT}\right)\left(s-s_\infty\right)+\tau\left[D_B\frac{\partial T}{\partial y}\frac{\partial c}{\partial y}+\frac{D_T}{T_\infty}\left(\frac{\partial T}{\partial y}\right)^2\right]$$
$$+\frac{\mu}{Scp}\left(\frac{\partial u}{\partial y}\right)^2+\frac{D_m KT}{Cs\,Cp}\frac{\partial^2 S}{\partial y^2} \tag{5}$$

$$u\frac{\partial S}{\partial x}+v\frac{\partial S}{\partial y}=D\frac{\partial^2 S}{\partial y^2}+\frac{DmKT}{T\infty}\frac{\partial^2 T}{\partial y^2}-K_r^2\left(s-s_\infty\right)\left(\frac{T}{T_\infty}\right)^n Exp\left(\frac{-E\alpha}{k\tau}\right) \tag{6}$$

Equation (5) depicts the conservation of thermal energy in the fluid by considering various heat transmission modes, such as convection and conduction. It defines the flow field's thermal energy transit and controls the boundary layer's temperature distribution. The conservation of solute concentration within the fluid, considering the effects of convection and molecular diffusion, is represented by Equation (6). It specifies the movement of species across the flow domain and controls the difference in concentration at the boundary layer.

$$v\frac{\partial c}{\partial y}+u\frac{\partial c}{\partial x}=\frac{D_T}{T_\infty}\frac{\partial^2 T}{\partial y^2}+D_B\frac{\partial^2 C}{\partial y^2} \tag{7}$$

Representing the solute concentration equation, which controls the dispersion and movement of species concentration in a fluid flow, is Equation (7). Convection and molecular diffusion work

together to point out how the concentration boundary layer forms, and this theory provides an explanation.

Equation from (1-7) are follows boundary conditions

$$\left.\begin{array}{l} D_\infty \dfrac{\partial c}{\partial y}+\dfrac{D_T}{T_\infty}\dfrac{\partial T}{\partial y}=0, v=0, S=S_\infty, T=T_w+T_{slip}; u=u_w+U_{slip}, \dfrac{\partial H_1}{\partial y}=1, H_2=0 \ at\ y=0 \\ C\to C_\infty, S\to S_\infty, T\to T_\infty, U\to 0, H_1\to H_0 x\ at\ y\to\infty \end{array}\right\} \quad (8)$$

The motion components in the stream wise and normal directions in the (x, y) plane are governed by the velocity boundary conditions specified for L_1 and L_2. This formulation is required for a correct description of the momentum distribution in the region of the boundary layer. These terms are removed to make the numerical values more stable, which helps in solving the boundary value problem with solvers such as bvp4c in MATLAB.

$$U_{slip}=L_1\frac{\partial u}{\partial y}, T_{slip}=L_2\frac{\partial T}{\partial y},\ q_r=-\frac{4\sigma^*}{3K'}\frac{\partial T^4}{\partial y}, \delta_1=\frac{\gamma_1}{2\pi}\frac{x}{x^2+(y+c)^2} \quad (9)$$

Where, U_{slip} - Velocity slip boundary condition and T_{slip} – energy slip boundary conditions

$$H_x=-\frac{\partial\delta_1}{\partial x}=\frac{\gamma_1}{2\pi}\frac{x^2-(y+c)^2}{(x^2+(y+c)^2)^2}, H_y=-\frac{\partial\delta_1}{\partial y}=\frac{\gamma_1}{2\pi}\frac{2x(y+c)}{(x^2+(y+c)^2)^2}. H=\sqrt{\left(\frac{\partial\delta_1}{\partial x}\right)^2+\left(\frac{\partial\delta_1}{\partial y}\right)^2} \quad (10)$$

Streamline Representation of the Fluid Flow

$$u=\frac{\partial\psi}{\partial y} \text{ and } v=-\frac{\partial\psi}{\partial x}$$

2.3 Similarity transformation

The controlling PDEs are transformed into ordinary differential equations using a similarity transformation, which involves the introduction of appropriate dimensionless variables. By simplifying the issue and allowing for an efficient numerical solution, this transformation keeps the important flow properties.

$$\psi=(a\nu)^{1/2}\, x f(\eta), f(\eta), u=cx\ f'(\eta),\ \ v=-\sqrt{c\nu}f(\eta) \quad (11)$$

The continuity equation presented in Eq. (1) is satisfied through the introduction of the similarity variable η and the stream functions ψ. Consequently, the corresponding transformed variables are expressed as follows.

$$H_1=H_0 x g'(\eta), H_2=-\sqrt{\frac{\nu}{c}}\ H_0 g(\eta), \eta=\sqrt{\frac{c}{\nu}}y,\ \theta(\eta)=\frac{T-T_\infty}{T_w-T_\infty}, \varphi(\eta)=\frac{C-C_\infty}{C_w-C_\infty}, \chi(\eta)=\frac{S-S_\infty}{S_w-S_\infty} \quad (12)$$

2.4 Numerical Simulation of Flow Behavior

By using similarity transformations, the system of governing equations Eqs. (1-4) is converted into a set of nonlinear ordinary differential equations Eqs. (13-17). Next, the numerical solution is applied to the resulting boundary value problem.

$$f'''+\lambda(\theta-N_r\varphi)-(f')^2+ff''+\beta\left((g')^2-gg''\right)=0 \quad (13)$$

$$\alpha_1 g'''+fg''-gf''=0 \quad (14)$$

$$P_r N_b\theta'\varphi'+P_r\sigma N_c\chi[1+\theta\delta]^n\, Exp\left[\frac{-E}{1+\theta\delta}\right]+P_r f\theta'+N_t P_r\theta'^2+P_r Ec(f'')^2 +\theta''\left[1+\frac{4}{3}Rd\right]+D_f\chi''=0 \quad (15)$$

$$\chi'' + Scf\,\chi' + ScSr\theta'' - Sc\sigma\chi\left(1+\theta\delta\right)^{n} Exp\left(\frac{-E}{1+\theta\delta}\right) = 0 \tag{16}$$

$$\varphi'' + \frac{N_t}{N_b}\theta'' + Scf\,\varphi' = 0 \tag{17}$$

2.5 Mathematical Model in Physical quantities

The physical factors that define the fluid's flow and heat transfer behavior are employed to formulate the governing equations. This model incorporates the effects of electro magneto hydrodynamics (EMHD), the Dufour effect, heat radiation, magnetic fields, and thermophoresis. Appropriate boundary conditions are applied to address the engineering problem effectively.

$$\left.\begin{aligned}
&\lambda = \frac{g\beta\rho f_\infty\left(1-C_\infty\right)\left(T_W-T_\infty\right)}{\rho_f C^2 x} = \frac{Gr_x}{\mathrm{Re}_x^2}, Gr_x = \frac{g\beta\rho f_\infty\left(1-C_\infty\right)\left(T_W-T_\infty\right)x^3}{v^2},\ \mathrm{Re}_x = \frac{u_w x}{v}\\
&\mathrm{Pr} = \frac{v_f}{\alpha_f}, Nb = \frac{\tau D_B C_\infty}{v_f},\ Rd = \frac{4\sigma^* T_\infty^3}{kK'},\\
&Nt = \frac{\tau D_T\left(T_w-T_\infty\right)}{T_\infty v_f},\ Sc = \frac{v_f}{D_B},\ \sigma = \frac{k_r^2}{C}, Nr = \frac{\left(\rho_p-\rho f_\infty\right)C_\infty}{\rho f_\infty\beta\left(1-C_\infty\right)\left(T_w-T_\infty\right)}\\
&E = \frac{E_\alpha}{KT_\infty},\ \delta = \frac{T_w-T_\infty}{T_\infty},\ Nc = \frac{\beta\left(S-S_\infty\right)}{T_w-T_\infty}, \beta = \frac{\mu H_0^{\,2}}{4\pi C^2\rho_f}, S_r = \frac{K_T D\left(T_w-T_\infty\right)}{vT_\infty\left(S_w-S_\infty\right)}, \alpha_1 = \frac{\mu_e}{v}.
\end{aligned}\right\} \tag{18}$$

$$\left.\begin{aligned}
&C_f = \frac{\tau_w}{\rho U^2}, Nu_x = \frac{xq_w}{k\left(T_f-T_\infty\right)}, Sh_x = \frac{xq_m}{D_s\left(C_w-C_\infty\right)}, Nn_x = \frac{xq_n}{D_B\left(\varphi_w-\varphi_\infty\right)}\\
&\tau_w = \mu\left[\partial u/\partial y\right]_{y=0}, q_w = -k\left[\partial T/\partial y\right]_{y=0}, q_m = -D_s\left[\partial C/\partial y\right]_{y=0}, q_n = -D_B\left[\partial\varphi/\partial y\right]_{y=0}\\
&C_f\left(\mathrm{Re}_x\right)^{\frac{1}{2}} = f''(0), \frac{Nu_x}{\left(\mathrm{Re}_x\right)^{\frac{1}{2}}} = -\theta'(0), \frac{Sh_x}{\left(\mathrm{Re}_x\right)^{\frac{1}{2}}} = -S'(0), \frac{Nn_x}{\left(\mathrm{Re}_x\right)^{\frac{1}{2}}} = -\gamma'(0)
\end{aligned}\right\} \tag{19}$$

3. Computational Framework and Analysis

The MATLAB solver bvp4c is utilized to numerically resolve the converted nonlinear ordinary differential equations and their corresponding boundary conditions. This solver is great at dealing with nonlinear boundary value issues since it uses a collocation-based method. To guarantee precision and convergence of numerical solutions, a relative tolerance of 10^{-6} is given.

$$\begin{aligned}
&f = y_1, f' = y_2, f'' = y_3, g = y_4, g' = y_5, g'' = y_6, \theta = y_7, \theta' = y_8,\\
&\varphi = y_9, \varphi' = y_{10}, \chi = y_{11}, \chi' = y_{12}
\end{aligned} \tag{20}$$

Using Eq. (20), Eq. (13)– (17) together with the corresponding boundary conditions in Eq. (18)– (19) are converted into the following system of first-order ODEs.

$$f''' = -\lambda\left(y_7 - N_r y_{11}\right) + y_2^2 - y_1 y_3 - \beta\left(y_5^2 - y_4 y_6\right) \tag{21}$$

$$g''' = \frac{1}{\alpha_1}\left[y_4 y_3 - y_1 y_6\right] \tag{22}$$

$$\theta'' = \frac{1}{\left(1+\frac{4}{3}Rd - D_f ScSr\right)}\left[\begin{aligned}
&D_f Scy_1 y_0 - P_r N_b y_8 y_{12} - P_r\sigma N_c y_9\left(1+y_7\delta\right)^n Exp\left(\frac{-E}{1+y_7\delta}\right)\\
&-\mathrm{Pr}\,y_1 {y_8}^2 - \mathrm{Pr}\,Ec\,{y_3}^2 - Sc\ \sigma y_9\left(1+y_7\delta\right)^n Exp\left[\frac{-E}{1+y_7\delta}\right]
\end{aligned}\right] \tag{23}$$

$$\chi'' = -Scy_1y_{10} + Sc\sigma y_9\left(1+y_7\sigma\right)^n - ScSr\left[\frac{1}{\left(1+\frac{4}{3}Rd - D_fScSr\right)}\left[\begin{array}{l} D_fScy_1y_0 - P_rN_by_8y_{12} - P_r\sigma N_cy_9\left(1+y_7\delta\right)^n Exp\left(\frac{-E}{1+y_7\delta}\right) \\ -\Pr y_1y_8{}^2 - \Pr Ec\, y_3{}^2 - Sc\ \sigma y_9\left(1+y_7\delta\right)^n Exp\left[\frac{-E}{1+y_7\delta}\right] \end{array}\right]\right] \quad (24)$$

$$\varphi'' = -Scy_1y_{12} - \frac{Nt}{Nb}\left[\frac{1}{\left(1+\frac{4}{3}Rd - D_fScSr\right)}\left[\begin{array}{l} D_fScy_1y_0 - P_rN_by_8y_{12} - P_r\sigma N_cy_9\left(1+y_7\delta\right)^n Exp\left(\frac{-E}{1+y_7\delta}\right) \\ -\Pr y_1y_8{}^2 - \Pr Ec\, y_3{}^2 - Sc\ \sigma y_9\left(1+y_7\delta\right)^n Exp\left[\frac{-E}{1+y_7\delta}\right] \end{array}\right]\right] \quad (25)$$

The problem formulation incorporates the following boundary conditions:

$$\left.\begin{array}{l} f\left(0\right)=0, f'\left(0\right)=1+L_1f''\left(0\right), g\left(0\right)=0, g''\left(0\right)=0, \theta\left(0\right)=1+L_2\theta'\left(0\right), \\ \varphi'\left(0\right)=-\left(\frac{Nt}{Nb}\right)\theta'\left(0\right), \chi\left(0\right)=1\, at\, \eta\to 0 \end{array}\right\} \quad (26)$$

$$f'\left(\infty\right)=0, g'\left(\infty\right)=1, \theta\left(\infty\right)=0, \phi\left(\infty\right)=0, \chi\left(\infty\right)=0\ at\, \eta\to\infty \quad (27)$$

3.1 Flow Diagram of the Numerical and Optimization Approach

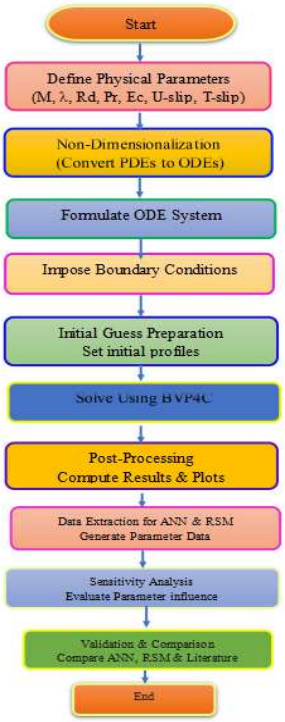


Fig. 3 Flow chart of the bvp4c solution procedure

4. Result and Discussion:

Table. 1 Comparison of the numerical values of the wall temperature gradient $\theta'(0)$ obtained in the present study with those reported by Mustafa et al [22] for M = 0.5, Nr = 0.5, δ = 1 and Sc = 5.

Pr	Nt	E	σ	n	λ	Present Value	Mustafa et al. [22]
2	0.5	1	1	0.5	0.5	0.767311	0.706605
4	-	-	-	-	-	0.943142	0.935952
7	-	-	-	-	-	1.134635	1.132787
10	-	-	-	-	-	1.267100	1.257476
5	0.1	1	1	0.5	0.5	1.432070	1.426267
-	0.5	-	-	-	-	1.039608	1.013939
-	0.7	-	-	-	-	0.853548	0.846943
-	1.0	-	-	-	-	0.648804	0.649940
10	0.5	1	2	0.5	0.0	1.034133	1.032281
0.5	-	-	-	-	-	1.057820	1.056704
3.0	-	-	-	-	-	1.155318	1.154539
5.0	-	-	-	-	-	1.216434	1.215937

4.1 Comparison of the present findings with existing studies

The current numerical formulation is validated by comparing the predicted Nusselt number values with the benchmark results reported by Mustafa et al. [22], which show excellent agreement, proving that the present method is both strong and accurate, for various Prandtl numbers under the conditions M = Nr = 0.5, δ = 1, and Sc = 5. The numerical results produced in this study show a very high level of agreement with the reference data. This shows that the computational scheme used is both accurate and reliable. The model's durability and ability to accurately describe the fundamental heat-transfer behavior are demonstrated by the continuous agreement seen throughout a broad range of Pr values. Additionally, this discovery is supported by the comparative data shown in Table 1, since the current predictions nearly match the published results in the literature. Such alignment supports the validity of the suggested analysis for forecasting heat transport characteristics and validates the methodological soundness of the current methodology.

Fig. 4 shows the effect of the velocity slip parameter (L_1=0.7 to 1.9) on the velocity profile, which clearly shows a decreasing-increasing pattern. The relaxation of the no-slip constraint, which reduces wall-fluid interaction, causes the near-wall velocity to decrease at lower slip values. This decrease is due to weaker momentum transfer from the surface. Because there is less shear resistance when L_1 increases, the fluid can accelerate more freely away from the wall. Consequently, velocity rises in the other boundary region. Overall, the profile exhibits a gradual increase following an initial decline, highlighting the conflicting effects of slip-induced momentum weakening near the wall and increased mobility farther from the surface. Fig. 5 shows how the strength of the magnetic dipole and the velocity-slip parameter affect the distribution of velocity. The induced Lorentz force gets stronger as the magnetic dipole intensity goes up. This force pushes against the fluid motion, which slows it down. This magnetic resistance makes it harder for momentum to move and makes the hydrodynamic boundary layer thicker. Increasing the velocity-slip parameter, on the other hand, makes the no-slip condition at the wall less strict. The fluid moves more freely along the surface when shear resistance is lower, and the speed near the boundary goes up. In general, Fig. 5 shows the competing effects: magnetic forces slow down the flow, while velocity slip speeds it up.

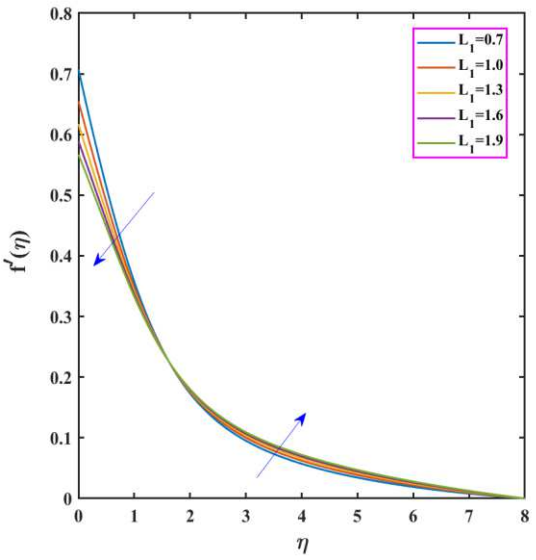


Fig. 4 Effect of velocity profile with velocity slip parameter

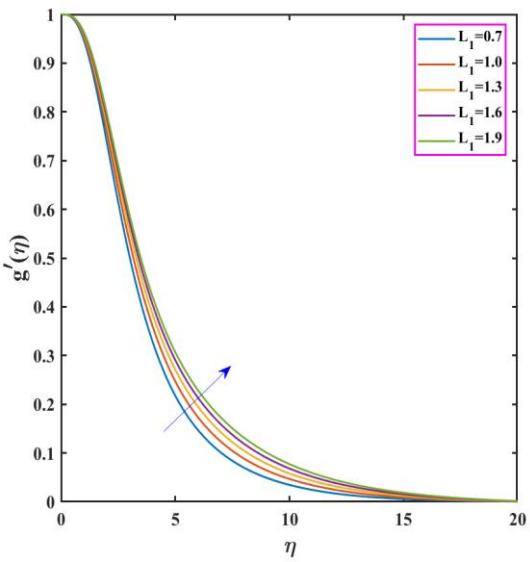


Fig. 5 Effect of velocity slip parameter with dipole profile

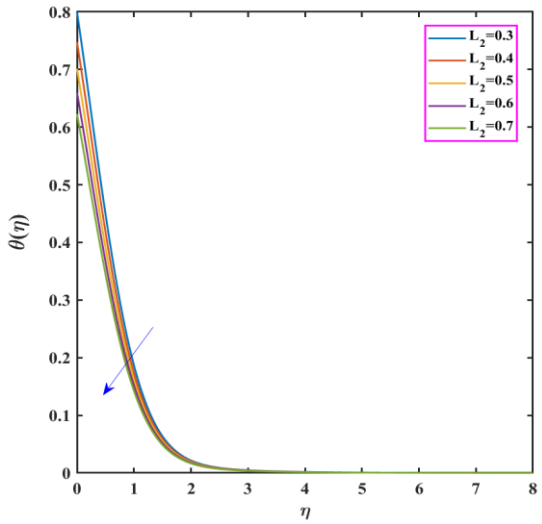


Fig. 6 Effect of energy slip parameter with temperature profile

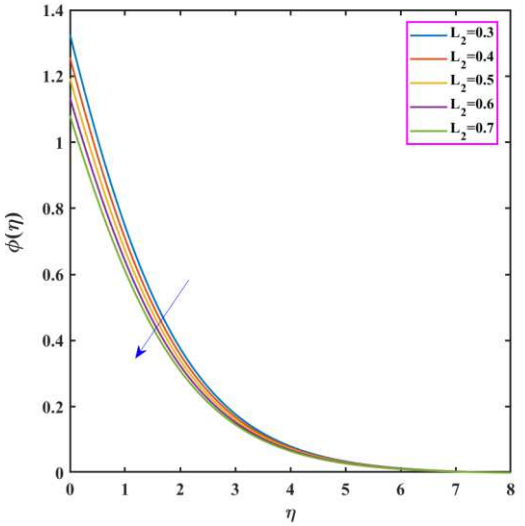


Fig. 7 Effect of energy slip parameter with concentration profile

Fig 6 shows how the energy profile changes when the energy-slip parameter is changed. The thermal interaction between the wall and the fluid gets weaker as the energy-slip condition goes up. This means that less heat is transferred from the surface. This weaker wall–fluid coupling lowers the temperature difference across the boundary layer and lowers the temperature distribution across the boundary layer. So, the thermal boundary layer gets thinner because the fluid gets less heat from the surface. The overall effect is that the energy profile gets noticeably lower as the slip intensity goes up. So, Fig. 6 clearly shows how energy slip stops heat transfer and lowers the temperature field of the fluid. Fig. 7 shows how the energy-slip parameter L_2 affects the concentration profile. As L_2 As the temperature rises, the thermal interaction between the wall and the fluid weakens, which slows down the transfer of heat from the surface. This drop in thermal energy near the boundary lowers the local temperature differences that usually cause mass diffusion due to heat. When thermal diffusion is weaker, the species transport mechanism loses some of its energy, which lets the boundary layer keep a higher concentration. Consequently, the concentration profile consistently ascends with the intensification of energy slip. In general, Fig. 7 shows that higher energy slip leads to higher concentration because the heat–mass coupling at the wall is weaker.

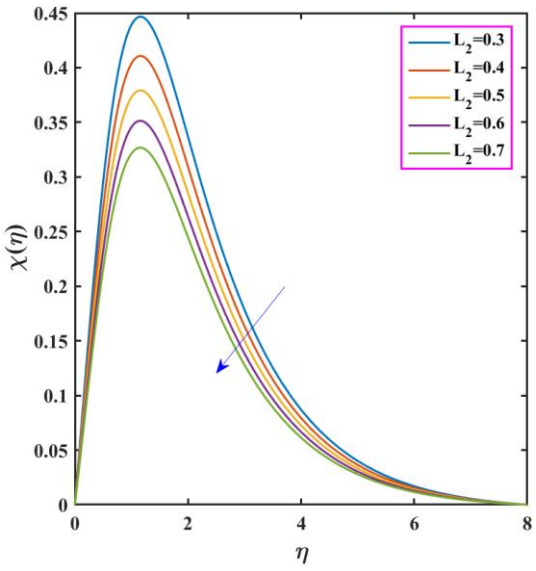


Fig. 8 Effect of energy slip parameter with solute concentration

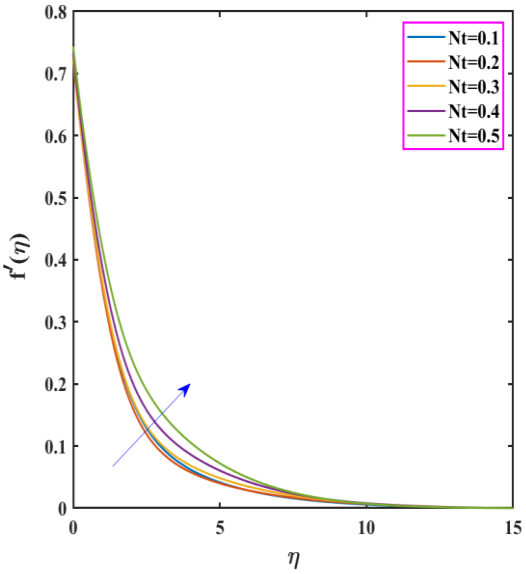


Fig. 9 Effect of thermophoresis parameter with velocity profile

Fig. 8 shows how the energy-slip parameter L_2 affects the profile of solute concentration. As L_2 The wall–fluid thermal interaction gets weaker as the temperature rises, which means that less heat is moved from the surface to the fluid. This decrease in heat input lowers the temperature differences that usually cause thermally assisted mass diffusion. The thermophoretic force acting on the solute particles is weaker in the near-wall region because there is less thermal energy there. This makes it harder for the particles to move toward the fluid domain. The concentration of the solute slowly decreases across the boundary layer as a result. In general, Fig. 8 shows that higher energy slip weakens the thermal driving forces that move species, which results in a lower concentration distribution. Figure 9 shows how the thermophoresis parameter affects the velocity profile. As the thermophoretic force gets stronger, particles that are moving because of temperature get stronger too. This makes particles that are suspended move away from the heated surface. This movement toward the outside lowers the number of particles near the boundary, which lowers the local fluid resistance. The effective viscosity in the near-wall region is lower because there are fewer particles blocking the motion. This lets the fluid move more freely. This makes the speed of the flow increase all the way through the boundary layer. In general, Fig. 9 shows that better thermophoresis speeds up the fluid by lowering particle-induced drag and making the fluid move more easily near the surface.

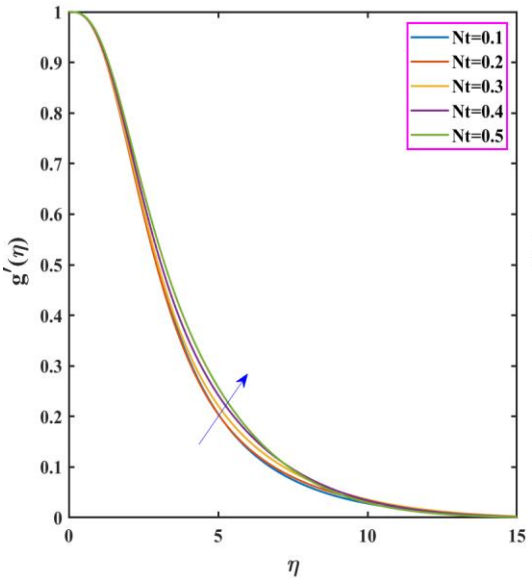


Fig. 10 Effect of thermophoresis with dipole profile

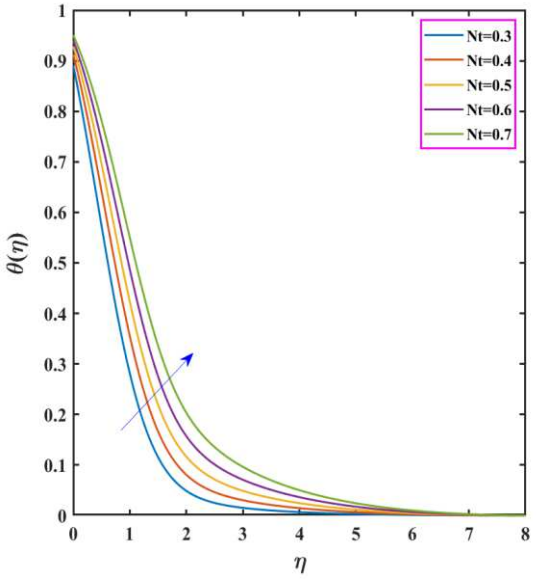


Fig. 11 Effect of thermophoresis parameter with energy profile

Fig. 10 illustrates the combined influence of thermophoresis and magnetic dipole strength on the flow field. As the thermophoresis parameter increases, temperature-driven particle migration away from the heated wall becomes stronger. This outward movement reduces particle accumulation near the surface and slightly enhances fluid motion. However, increasing the magnetic dipole produces a stronger Lorentz force that opposes the fluid flow. This magnetic resistance suppresses momentum transfer and reduces the velocity in the boundary layer. The two effects therefore act competitively, with thermophoresis supporting flow enhancement while the magnetic dipole induces flow retardation. Overall, Fig. 10 shows how these opposing mechanisms jointly control the velocity distribution. Fig. 10 illustrates the effect of the thermophoresis parameter on the temperature distribution. As the thermophoresis parameter increases, the temperature-driven migration of particles away from the heated surface becomes more significant. This movement reduces particle clustering near the wall, allowing more thermal energy to remain within the fluid rather than being absorbed by the particles. As a result, the fluid retains a higher temperature throughout the boundary layer. The reduced particle–wall interaction also weakens heat removal from the fluid, further elevating the temperature field. Consequently, the temperature profile rises consistently with increasing thermophoresis intensity. Overall, Fig. 11 highlights how thermophoresis enhances the fluid's thermal energy retention and leads to a higher temperature distribution.

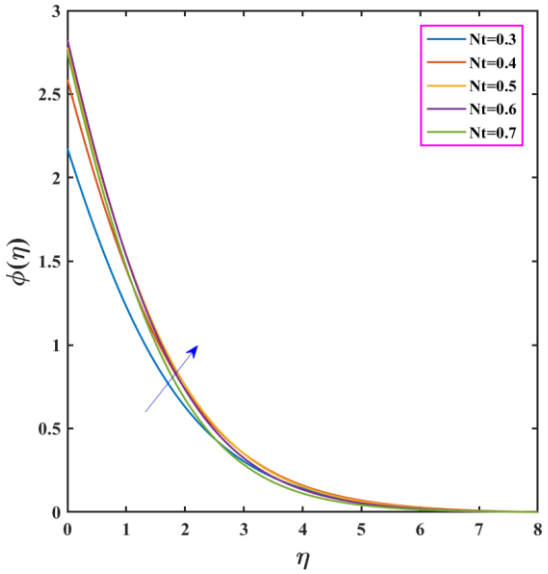


Fig. 12 Effect of thermophoresis parameter with concentration profile

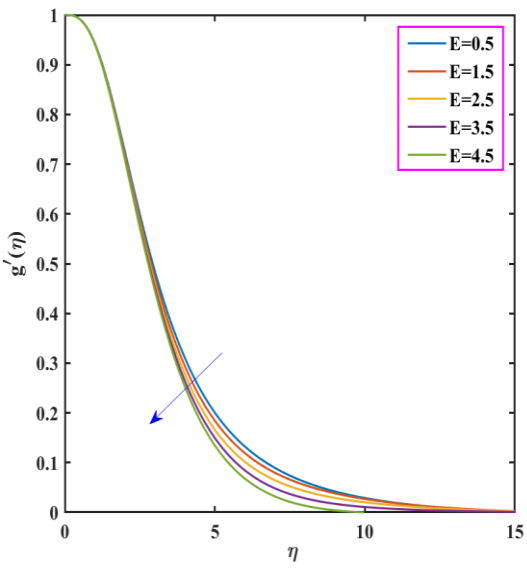


Fig. 13 Effect of thermophoresis parameter with activation energy profile

Figure 11 shows how the thermophoresis parameter changes the concentration profile. The temperature gradient in the boundary layer becomes better at moving particles as the thermophoresis parameter goes up. This stronger thermophoretic force moves the solute particles away from the heated wall and spreads them out more evenly throughout the fluid region. The overall concentration level goes up because the particles are moved deeper into the boundary layer. The lower number of particles near the surface also weakens diffusive losses to the wall, which supports the rise in concentration even more. So, higher thermophoresis makes the concentration profile go up a lot. Overall, Fig. 12 shows how thermophoresis improves the movement of species and the spread of solutes. As the activation energy parameter goes up, the dipole-induced concentration profile goes down, as shown in Fig. 13. A higher activation energy makes it harder for molecules to diffuse and react with each other. This means that particles need more energy to get past this barrier. This makes it harder for species to move around, which makes the dipole-driven transport in the boundary layer weaker. As a result, the concentration boundary layer gets thinner, and the overall dipole profile gets weaker because diffusion activity is stopped.

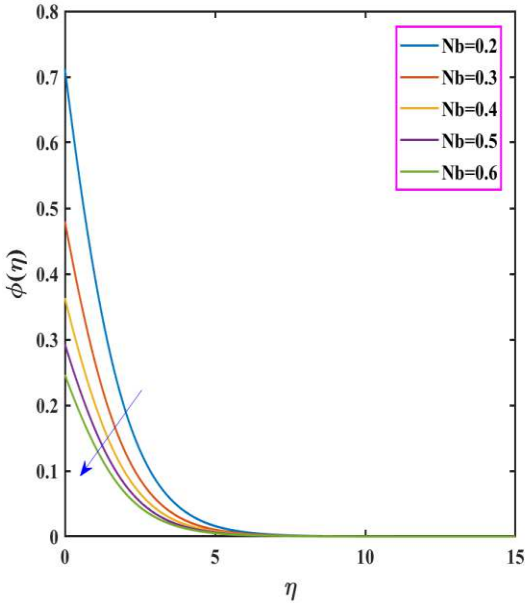


Fig. 14 Effect of Brownian motion parameter with concentration profile.

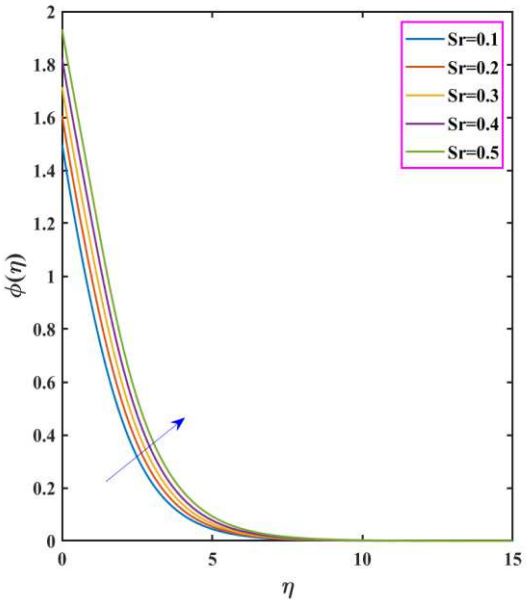


Fig. 15 Effect of Soret number with concentration profile

Figure 14 shows that the concentration profile goes down as the Brownian motion parameter (Nb) goes up. A higher Nb makes nanoparticles move more randomly in the fluid, which makes them spread out more quickly from the wall area. This increased microscopic agitation stops species from building up near the boundary, which lowers the local concentration. The concentration boundary layer gets thinner as a result. This means that stronger Brownian diffusion helps particles spread out and lowers the overall concentration distribution in the flow field. Fig. 15 shows that the concentration profile goes up as the Soret parameter (Sr) goes up. A higher Soret parameter makes the thermophoretic mass flux stronger when there are temperature differences. This stronger thermal-diffusion effect moves more solute particles from areas of higher temperature to areas of lower temperature. This causes species to build up in the boundary layer. As a result, the concentration boundary layer gets thicker and the overall concentration level rises. This shows that thermal-driven mass transfer is the main force when the Soret effect gets stronger.

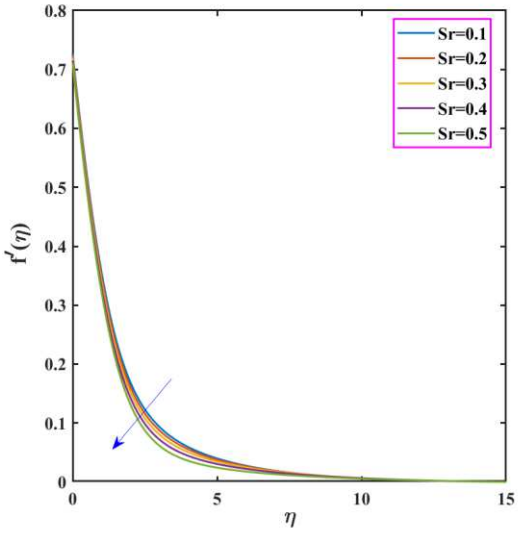


Fig. 16 Effect of Soret number with velocity profile

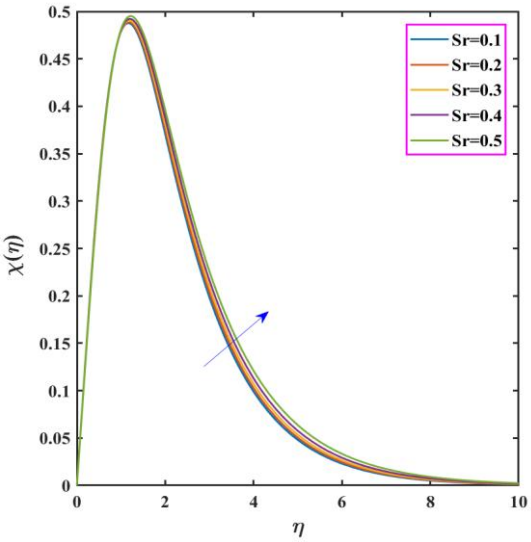


Fig. 17 Effect of Soret number with solute concentration profile

Figure 16 shows that the velocity profile gets lower as the Soret parameter (Sr) goes up. The Soret effect makes mass diffusion stronger when there are temperature differences, which makes solute particles move around more in the fluid. This increased mass transport changes the way the fluid's

density is spread out and adds more resistance to the flow that is caused by diffusion. Because of this, the fluid's momentum is lessened, and the velocity boundary layer gets thinner. So, higher Sr values slow down the flow of the fluid, which makes the velocity profile across the boundary layer much lower. Fig. 17 illustrates how the solute concentration profile rises as the Soret parameter (Sr) does. The thermal-diffusion (Soret) effect, in which temperature gradients actively push solute particles from hotter to cooler locations, is physically enhanced by a greater Sr. More solute species accumulate in the border layer because of this thermally induced mass movement. Consequently, the total concentration level increases and the concentration boundary layer thicken. As a result, raising Sr increases the temperature-driven mass flux, which improves the flow field's solute concentration distribution.

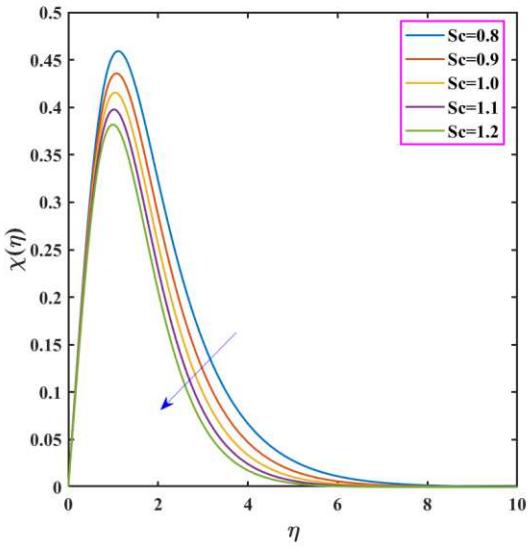


Fig. 18 Effect of Schmidt number with solute concentration profile

The solute concentration profile falls as the Schmidt number (Sc) rises, as shown in Fig. 18. The ratio of momentum diffusivity to mass diffusivity is represented physically by the Schmidt number. Lower mass diffusivity, or slower solute particle diffusion through the fluid, is correlated with a higher Sc. The capacity of species to disperse from the wall region is restricted by this decrease in molecular diffusion. Consequently, the total solute concentration falls, and the concentration boundary layer thins. Consequently, a lower concentration distribution within the border layer results from rising Sc suppressing mass movement.

4.2 RSM Methodology

Response Surface Methodology (RSM) is a powerful statistical tool for developing and optimizing processes by exploring the relationships between several input factors and one or more output responses. It employs planned experiments, such as central composite and Box–Behnken designs, to generate a polynomial equation to model the actual response surface. The model assists RSM to identify the significant factors and their interactions and the response behavior is visualized through contour and 3D surface plots. In the end, the RSM allows efficient optimization towards maximum, minimum or targeted responses with fewer experimental trials and better overall understanding of the process.

Table-2. RSM Input Parameter Levels: Velocity Slip, Energy Slip, and Thermophoresis

Parameters	Low (-1)	Middle (0)	High (1)
$0.6<L_1<1.1$	0.6	0.85	1.1
$0.2<L_2<0.7$	0.2	0.45	0.7
$0.01<Nt<0.5$	0.01	0.255	0.5

Table-3. Performance Characteristics of Skin Friction and Nusselt Number Under Parametric Variations

Run	Coded values			Actual values			$C_f(Re_x)^{0.5}$	$Nu\ (Re_x)^{-0.5}$
	A	B	C	L_1	L_2	Nt		
1	-1	-1	-1	0.6	0.2	0.01	-0.7578	-0.6353
2	1	-1	-1	1.1	0.2	0.01	-0.3952	-1.0252
3	-1	1	-1	0.6	0.7	0.01	-1.0081	-0.8893
4	1	1	-1	1.1	0.7	0.01	-0.6455	-1.2793
5	-1	-1	1	0.6	0.2	0.5	-0.8074	-0.5072
6	1	-1	1	1.1	0.2	0.5	-0.4448	-0.8972
7	-1	1	1	0.6	0.7	0.5	-1.0607	-0.7601
8	1	1	1	1.1	0.7	0.5	-0.6981	-1.1501
9	-1	0	0	0.6	0.55	0.255	-0.9298	-0.7343
10	1	0	0	1.1	0.55	0.255	-0.5672	-1.1243
11	0	-1	0	0.85	0.2	0.255	-0.6109	-0.8537
12	0	1	0	0.85	0.7	0.255	-0.8641	-1.1067
13	0	0	-1	0.85	0.55	0.01	-0.7417	-0.9300
14	0	0	1	0.85	0.55	0.5	-0.7928	-0.8026
15	0	0	0	0.85	0.55	0.255	-0.7665	-0.8663
16	0	0	0	0.85	0.55	0.255	-0.7665	-0.8663
17	0	0	0	0.85	0.55	0.255	-0.7665	-0.8663
18	0	0	0	0.85	0.55	0.255	-0.7665	-0.8663
19	0	0	0	0.85	0.55	0.255	-0.7665	-0.8663
20	0	0	0	0.85	0.55	0.255	-0.7665	-0.8663

To make the regression analysis easier, the chosen parameters were given specific ranges of variation and then coded into three qualitative levels: low (–1), middle (0), and high (+1), as shown in Table 2. This coded representation is very important for making response surface models because it makes it possible to systematically find combinations of parameters that need to be carefully tested through numerical simulations or experimental runs. The selected ranges were meticulously delineated to guarantee that the resultant model accurately reflects the system behavior within the anticipated limits of skin friction and heat transfer, thereby enhancing the precision of surface fitting and predictive efficacy. For RSM analysis to be useful and process optimization to work, structured coding is necessary. This is shown more clearly in the tables that follow.

Table 3 shows the response surface methodology (RSM) simulation runs, with both the coded and uncoded values of the main input parameters. It has the skin friction coefficient and Nusselt number outputs that go with it, which lets you fully see how changes in the governing parameters affect heat transfer and frictional resistance. The information in this table makes it easier to understand the regression models by giving us the real-world examples we need to judge how reliable their predictions are. In this situation, Table 3 shows the empirical strategy used in the study, which is based on the systematic design of simulations based on the given parameter levels. In general, it is an important step in the empirical modeling framework because it connects the physical phenomena being studied with the regression equations that were created and checks these equations against the simulation results that were seen.

Table 4 ANOVA Table for Skin Friction Response (Cf)

Source	DF	Adj SS	Adj MS	F-Value	P-Value	Is this significant?
Model	9	0.012261	0.001362	222.89	0.000	Yes
Linear	3	0.002087	0.000696	113.84	0.000	Yes
L_1	1	0.000062	0.000062	10.08	0.010	Yes
L_2	1	0.000638	0.000638	104.38	0.000	Yes
Nt	1	0.001388	0.001388	227.07	0.000	Yes
Square	3	0.000512	0.000171	27.92	0.000	Yes
$L_1 * L_1$	1	0.000206	0.000206	33.75	0.000	Yes
$L_2 * L_2$	1	0.000000	0.000000	0.00	0.979	No
Nt*Nt	1	0.000255	0.000255	41.73	0.000	Yes
2-Way Interaction	3	0.009661	0.003220	526.90	0.000	Yes
$L_1 * L_2$	1	0.005455	0.005455	892.49	0.000	Yes
L_1 ***Nt**	1	0.003574	0.003574	584.81	0.000	Yes
L_2 ***Nt**	1	0.000632	0.000632	103.39	0.000	Yes
Error	10	0.000061	0.000006			
Lack-of-Fit	5	0.000061	0.000012			
Pure Error	5	0.000000	0.000000			

Regression	R^2	Adjusted R^2	Predicted R^2	Adeq Precision
	0.9991	0.9990	0.9984	511.7001

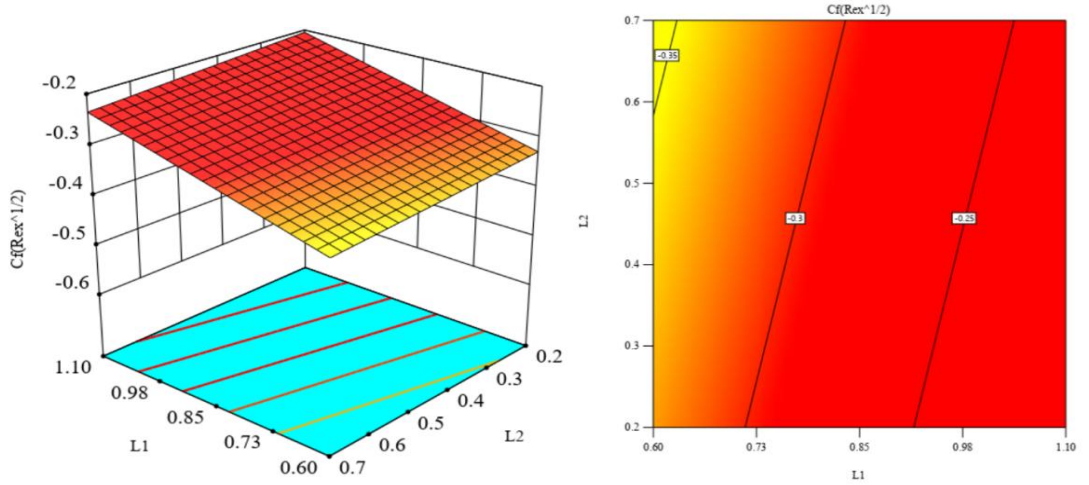
Table 4 shows the results of the ANOVA test that was used to check the regression model. It gives the degrees of freedom, the sum of squares, the mean squares, the F-values, and the levels of significance. The very low p-values and the "Yes" markings in the significance column show that all the main effects, including linear, quadratic, and interaction terms, are statistically significant. The high R^2 (0.9991) value shows that the model can make good predictions. Also, the low lack-of-fit and pure error values show that the model fits the data well within the ranges of the parameters that were tested. Table 4 clearly shows that the regression model for skin friction in the MHD nanofluid flow is both statistically sound and useful for making predictions.

Table 5 ANOVA Table for Nusselt number Response (Nu)

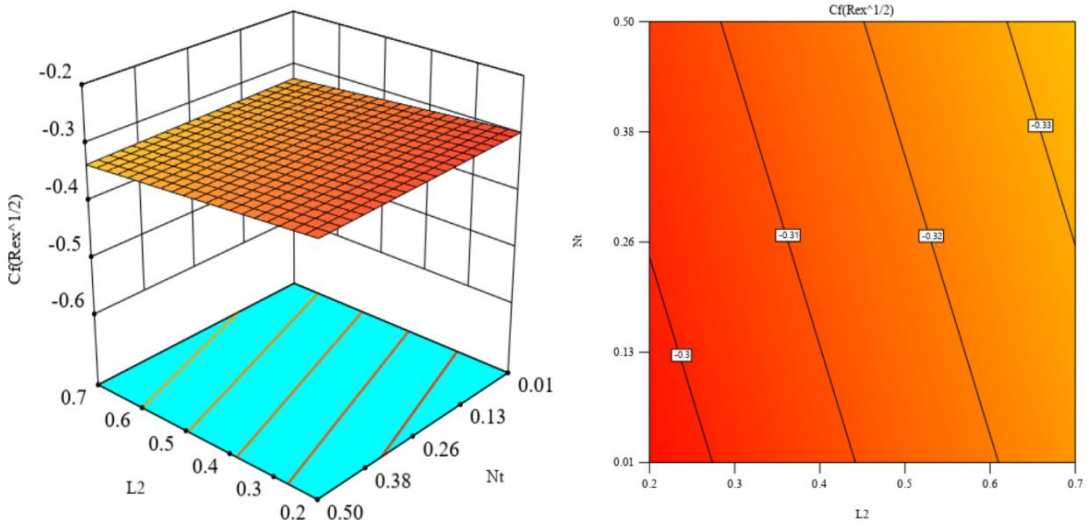
Source	DF	Adj SS	Adj MS	F-Value	P-Value	Is this significant?
Model	9	0.049652	0.005517	481.67	0.000	Yes
Linear	3	0.003055	0.001018	88.92	0.000	Yes
L_1	1	0.000052	0.000052	8.50	0.020	Yes
L_2	1	0.000001	0.000001	6.06	0.039	Yes
Nt	1	0.003003	0.003003	262.20	0.000	Yes
Square	3	0.028365	0.009455	825.50	0.000	Yes
$L_1 * L_1$	1	0.010036	0.010036	876.25	0.000	Yes
$L_2 * L_2$	1	0.013187	0.013187	1151.33	0.000	Yes
Nt*Nt	1	0.002692	0.002692	235.05	0.000	Yes
2-Way Interaction	3	0.018231	0.006077	530.59	0.000	Yes
$L_1 * L_2$	1	0.001105	0.001105	96.43	0.000	Yes
L_1 ***Nt**	1	0.010153	0.010153	886.46	0.000	Yes

L_2 *Nt	1	0.006974	0.006974	608.87	0.000	Yes
Error	10	0.000115	0.000011			
Lack-of-Fit	5	0.000115	0.000023			
Pure Error	5	0.000000	0.000000			
Regression	R^2	Adjusted R^2	Predicted R^2	Adeq Precision		
	0.9993	0.9992	0.9992	457.9112		

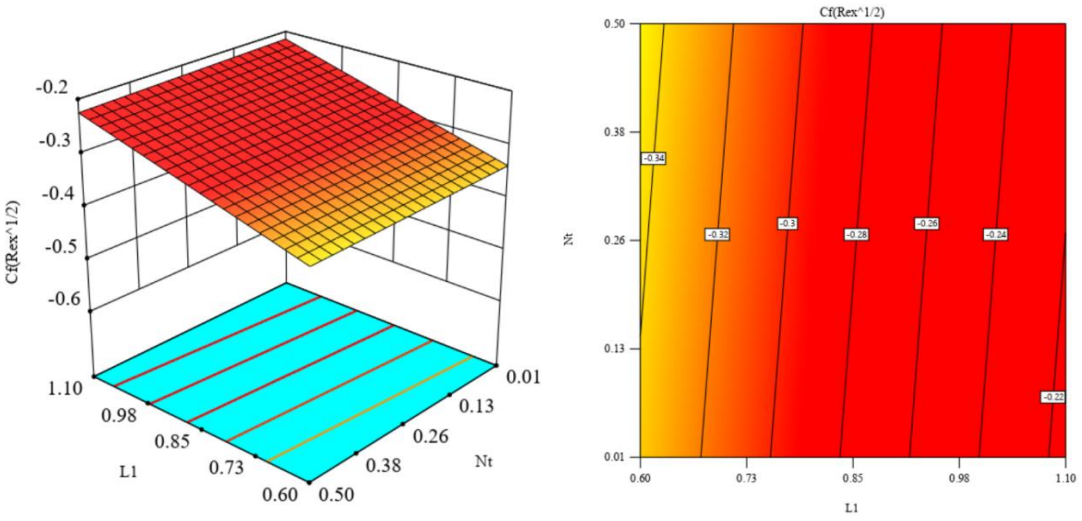
Table 5 shows the results of the Nusselt number regression model ANOVA, which shows how much each linear, square, and interaction term added to the model. The F-statistics and p-values for each model component show that they all have a big effect on the model, which is in line with how heat transfer works. And all the p values (less than 0.05) and F-statistics also show that they made a big difference. The minimal lack of fit and plain error also shows that the model fits the tested region well. The very high R^2, adjusted R^2, and predicted R^2 values (0.9993) show that the fit is very close. The model performs well within the tested range, as seen by the low lack-of-fit and pure error scores. Additionally, the strong R^2 value demonstrates how well the model predicts the data. Overall, the primary parameters' effects on the heat-transfer response are clearly reflected in the regression model. Because of this, the model is trustworthy and appropriate for additional optimization and sensitivity analysis in the MHD nanofluid system under study.



(a) **(b)**



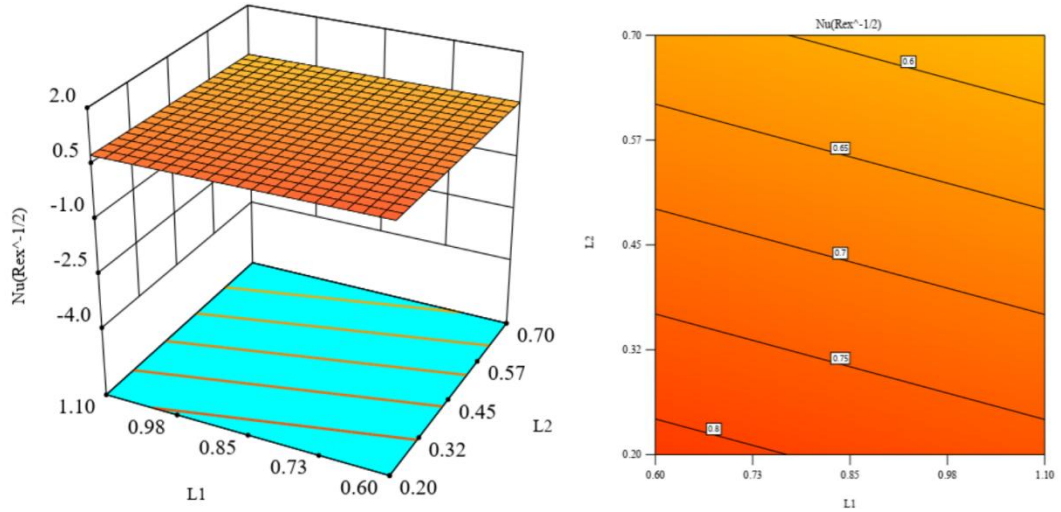
(c) **(d)**



(e) **(f)**

Fig. 19 Combined 3D surface plots(a,c,e) and 2D contour plots(b,d,f) analysis of L_1 , L_2 and Nt effects on skin friction.

Fig. 19 illustrates the influence of the velocity slip parameter (L_1) and the energy slip parameter (L_2) on the skin-friction coefficient (Cf), presented through 3D surface plots (a, c, e) and their corresponding 2D views (b, d, f). Increasing the slip parameters physically weakens the no-slip behavior at the wall by decreasing the fluid's adhesion to the surface. Cf decreases when L_1 rises because of the decreased momentum transfer at the boundary, which lowers the wall shear stress. Higher L_2 also reduces the shear at the wall and indirectly modifies the momentum boundary layer structure by weakening the thermal connection between the fluid and the surface. While the 2D views emphasize the rate of decrease in skin friction with respect to each slip parameter, the 3D surfaces clearly demonstrate the combined nonlinear influence of L_1 and L_2 on Cf. These patterns demonstrate that increased slip effects reduce the skin-friction coefficient and weaken wall resistance.



(a) **(b)**

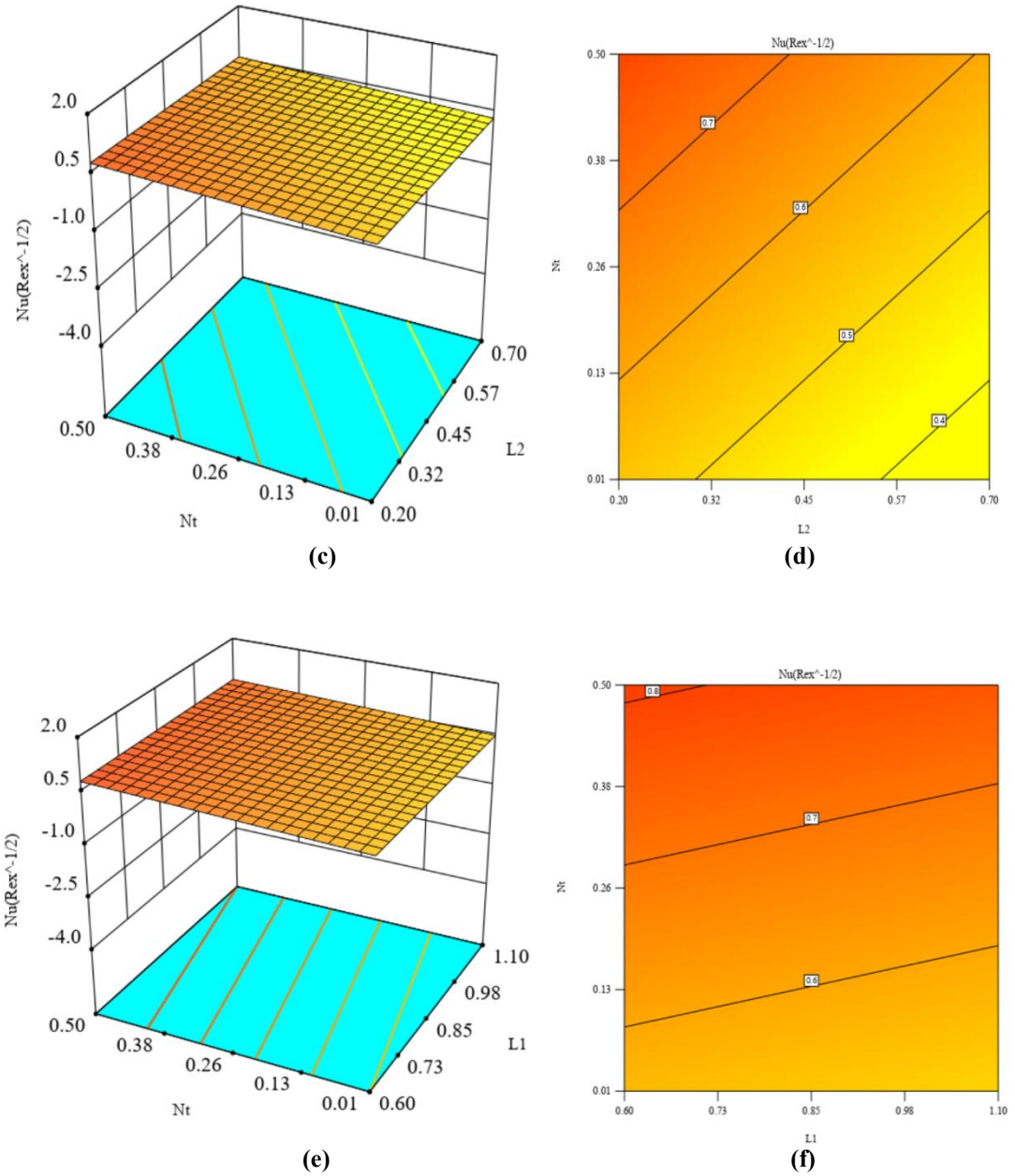


Fig. 20 Combined 3D surface plots(a,c,e) and 2D contour plots(b,d,f) analysis of L_1 , L_2 and Nt effects on Nusselt number.

Fig. 20 presents the effect of the velocity slip parameter (L_1) and the energy slip parameter (L_2) on the Nusselt number (Nu), illustrated through 3D surface plots (a, c, e) and the corresponding 2D views (b, d, f).Nu decreases when L_1 rises because of the decreased fluid–wall contact, which reduces the convective heat transfer strength. Similarly, a greater energy slip parameter L_2 reduces the heat flow transported from the surface to the fluid by relaxing the thermal boundary condition at the wall. The Nusselt number further decreases because of the smaller thermal boundary layer contribution to heat exchange. While the 2D graphs make it evident how quickly heat-transfer efficiency declines, the 3D surfaces show Nu's combined sensitivity to both slip parameters. The wall heat-transfer rate is generally decreased by greater slip effects, as indicated by the declining Nusselt number.

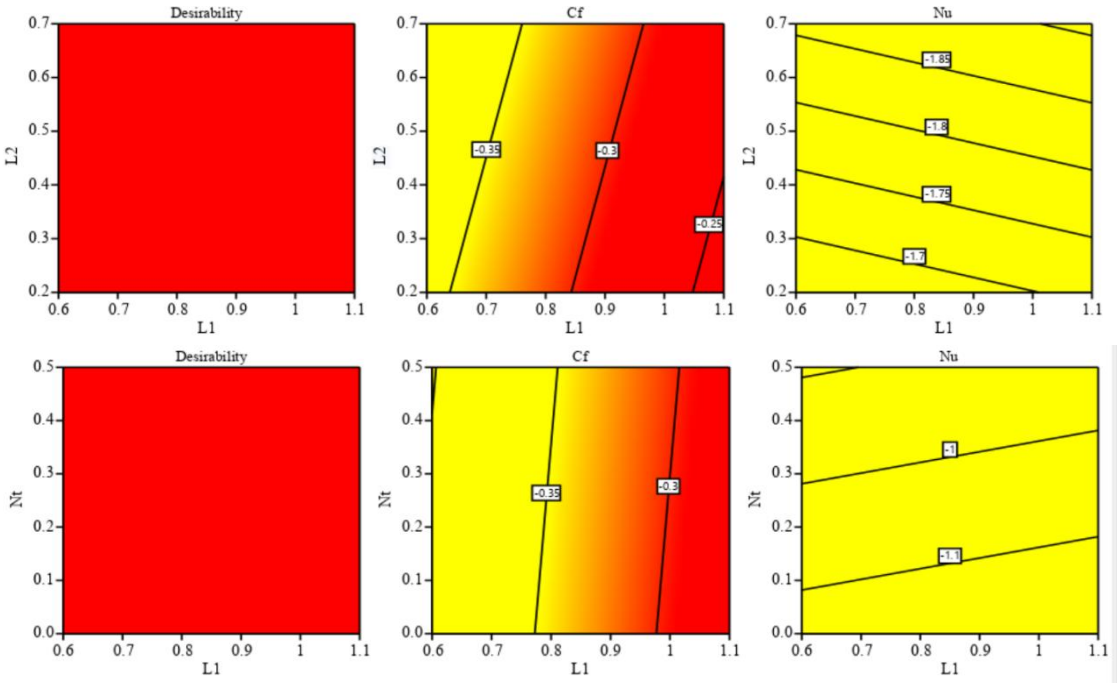
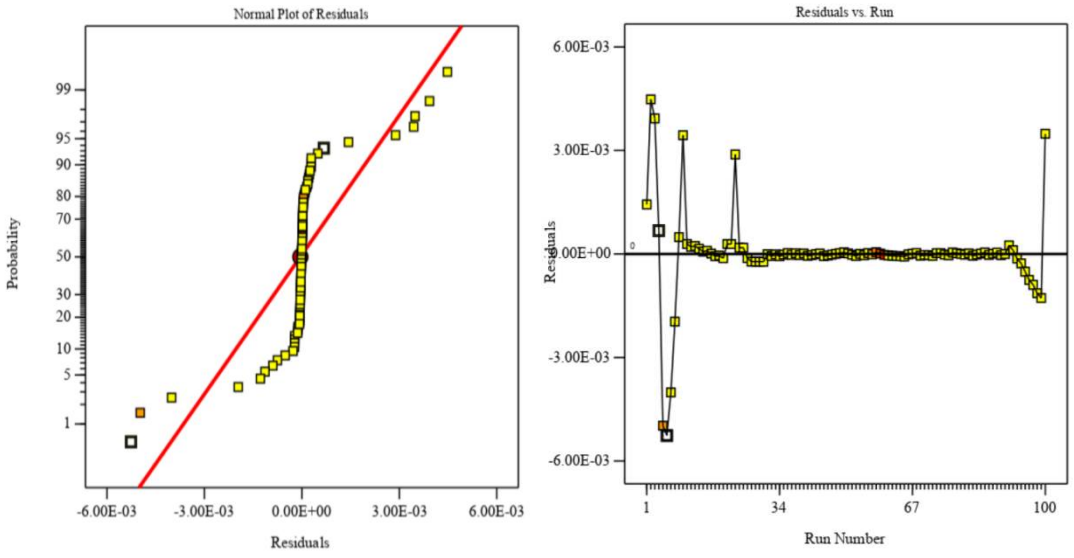
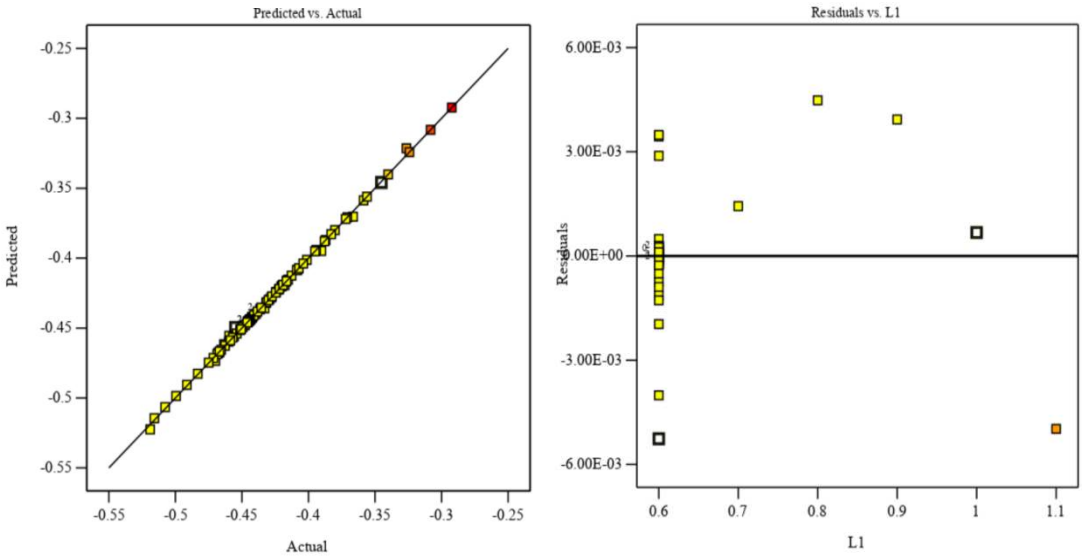


Fig. 21 RSM-Based Desirability plots for Skin friction and Nusselt Responses

Fig 21 shows the slip parameters increase, the momentum and thermal interactions at the wall weaken, reducing the rate of heat transfer from the surface. When the slip parameters go up, the momentum and thermal interactions at the wall get weaker, which slows down the rate at which heat moves from the surface. The Nu value goes down because the wall shear and temperature gradient go down. This means that maximizing heat transfer is less desirable. On the other hand, raising the thermophoresis parameter makes the particle-driven heat transport mechanism work better, which helps move thermal energy away from the heated surface. This effect can help make up for some of the loss caused by slip conditions. The desirability plot shows this competition by showing areas where good combinations of slip and thermophoresis parameters lead to higher Nu values, which means better heat transfer.



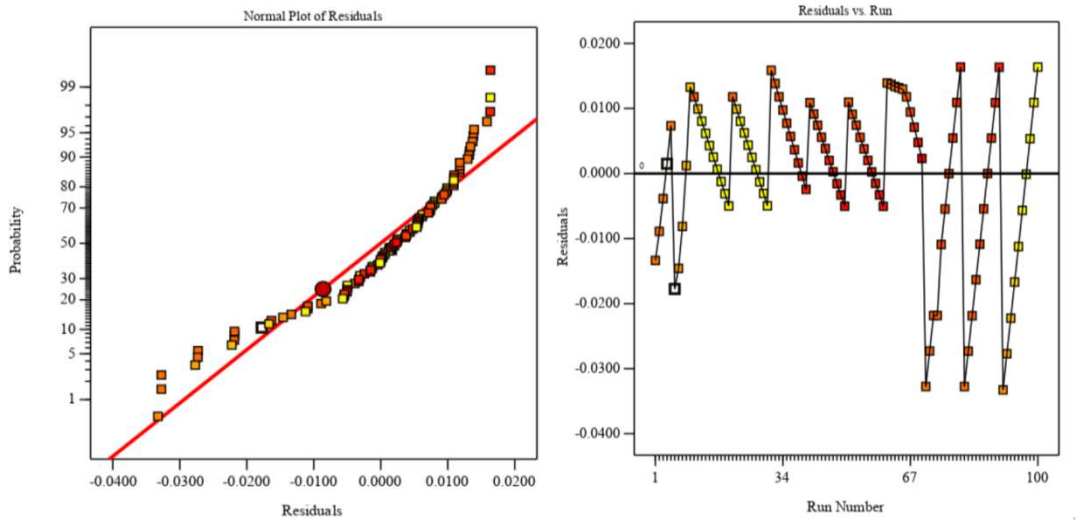
(a) **(b)**



(b) **(d)**

Fig. 22. Diagnostic Residual Plots Illustrating Cf behavior (a–d)

Fig 22 shows the overall diagnostic behavior of the created model using several statistical plots. The normal probability plot indicates that the residuals follow a trend that is almost a straight line. This means that the errors are normally distributed and the model is statistically sound. The distribution of the residuals also seems random and uniformly spread out around zero, which means that the variance is constant and there is no heteroscedasticity. The residual vs. runs figure further verifies that there was no drift overtime or a trend that happened repeatedly during the simulations or tests, which means the data is stable. Most data points in the projected vs. actual plot are near the 45° reference line, indicating a high degree of agreement between the model's predictions and actual values. Furthermore, there is no discernible trend in the residuals vs. L_1 velocity slip boundary condition plot, demonstrating that the model correctly depicts the physical impact of velocity slip throughout its range and that changes in the slip parameter do not induce bias. All things considered, the statistical evidence confirms that the model is dependable, consistent, and appropriate for forecasting the behavior of the system.



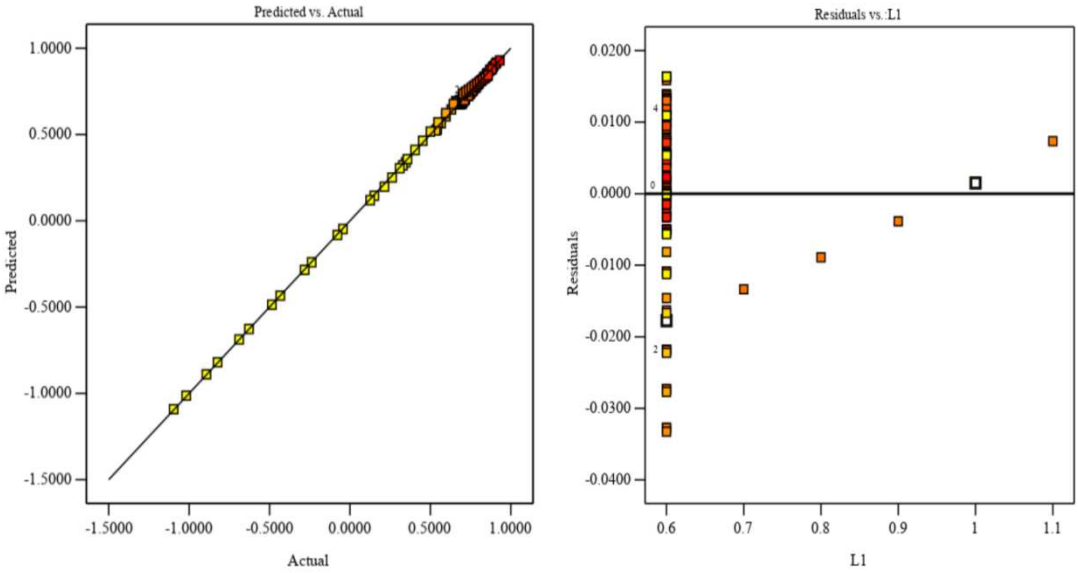


Fig. 23. Diagnostic Residual Plots Illustrating Nu behavior (a–d)

Fig 23 shows the statistical validity of the Nusselt number (Nu) predictive model. The points in the normal probability plot of residuals exhibit a virtually straight-line trend, indicating that the Nu model assumptions are met and the errors are normally distributed. The distribution of residuals looks random and equally distributed, suggesting constant variance and verifying that the model does not exhibit bias when estimating heat-transfer behavior. The evaluation of Nu is stable and unaffected by time-dependent numerical drift, as demonstrated by the residuals vs. runs plot, which displays no regular trend throughout the series of computational or experimental runs. Strong agreement between the model predictions and real Nusselt number values is indicated by the predicted vs. actual plot, which shows that the data points are near the ideal diagonal line. Additionally, the residuals vs. L_1 velocity slip boundary condition plot shows a random scatter, indicating that the influence of velocity slip on Nu is accurately represented and that changes in the slip value do not generate model errors. When taken as a whole, these diagnostic graphs demonstrate the established model's statistical dependability and accuracy in predicting the Nusselt number under various slip and flow conditions.

4.1 Development of the ANN-Based Prediction Model

The ANN architecture is depicted in Fig 24, which also shows how the input, hidden, and output layers interact. All the chosen process variables are received by the input layer, which then uses weighted connections to send them to the hidden neurons. Each neuron in the buried layer uses a nonlinear activation function and weighted summation to capture intricate correlations in the data. After processing, these signals are sent to the output layer, where the network produces the anticipated response. This structure shows how the nonlinear behavior between input parameters and output variables is efficiently mapped by the ANN.

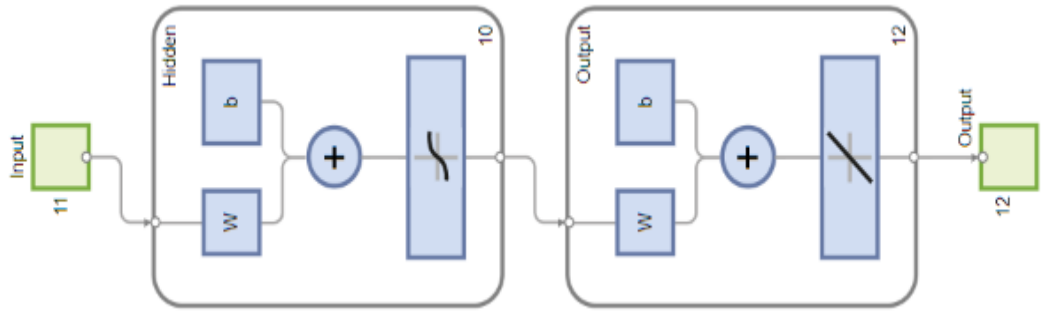


Fig. 24 Schematic diagram of the designed ANN model structure.

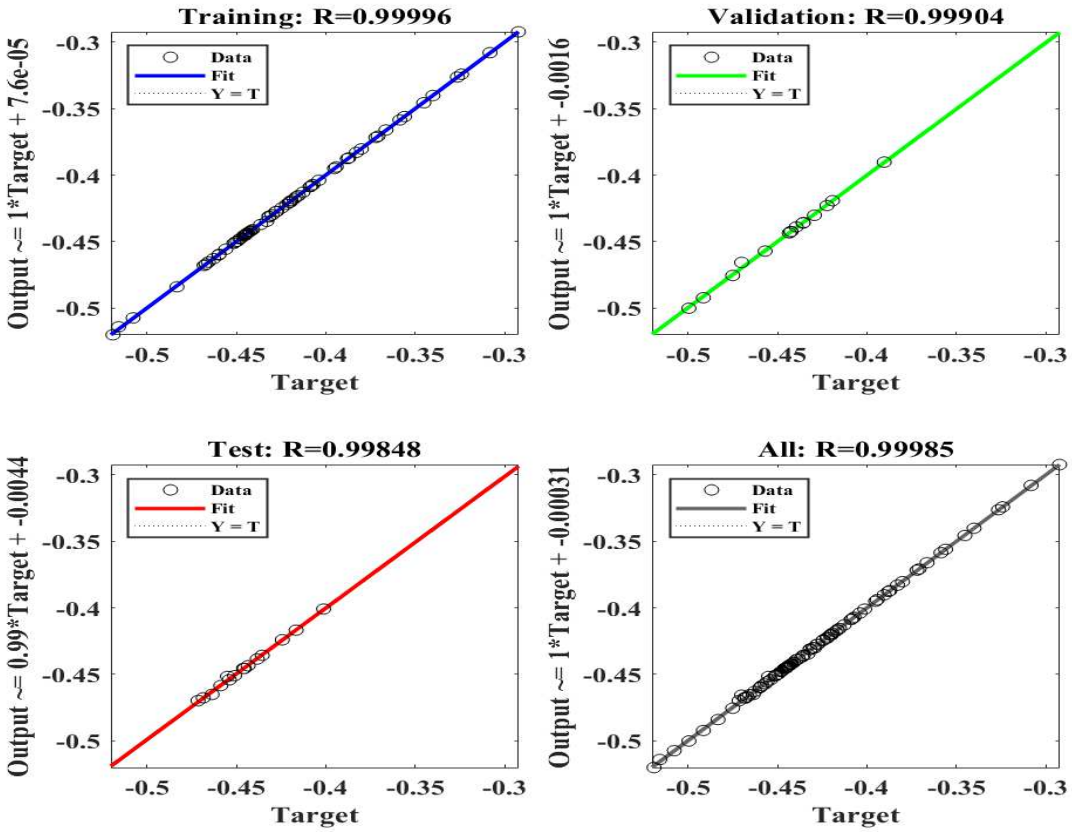


Fig. 25 Skin friction and Nusselt number regression performance based on ANN/RSM

Fig 25 shows the regression plots that came from the trained ANN model for predicting skin friction and the Nusselt number. The data points in the regression graph show that there is a strong linear relationship between the ANN-predicted outputs and the target values because they are all very close to the reference diagonal line. This close alignment shows that the model has successfully captured the nonlinear interactions between the input parameters and the flow physics. The ANN's excellent regression performance shows that it can be used to model complex slip-flow and thermal transport phenomena since it gives accurate and reliable estimates of both skin friction and heat-transfer rate.

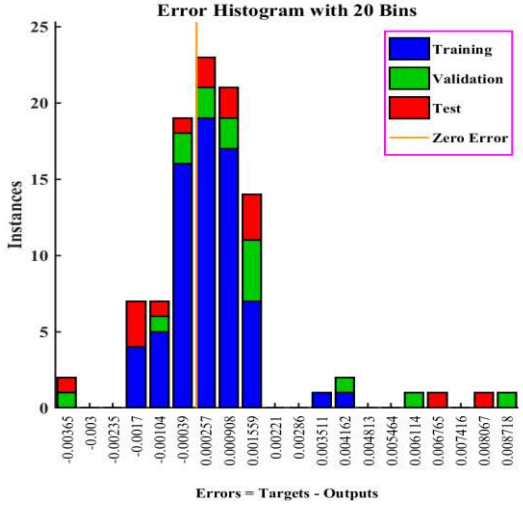


Fig. 26 Error Spread Visualization for Model Performance Assessment

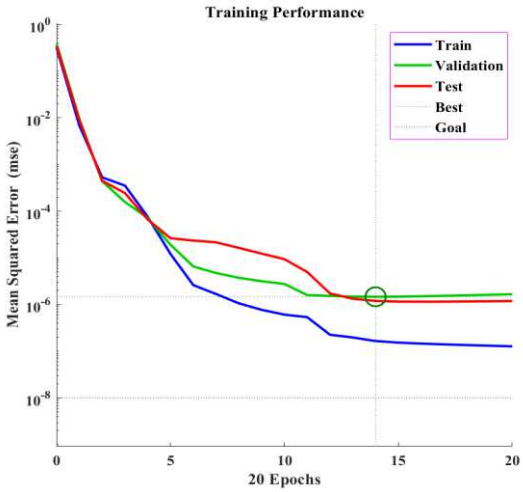


Fig. 27 Epoch-Wise Reduction in MSE for the ANN Model

The Artificial Neural Network (ANN) error histogram, which depicts the distribution of prediction errors between the network outputs and the target values, is shown in Fig 26. The ANN model has successfully learned the underlying physical relationships and generates extremely accurate predictions when most mistakes are concentrated around zero. Both under-prediction and over-prediction are negligible when the error distribution is symmetric and narrow, indicating that the model is not significantly biased. The lack of long tails or severe error bars further demonstrates that the ANN performs reliably under various input conditions and generalizes effectively to the provided dataset.

The Epoch vs. Mean Squared Error (MSE) plot in Fig 27. shows how the Artificial Neural Network (ANN) learns during training. The MSE steadily drops as the number of epochs rises, demonstrating how the network constantly modifies its weights to reduce prediction error. The ANN's capacity to accurately capture the underlying physical relationships in the data without instability or oscillation is confirmed by the smooth decreasing trend. The network has reached an optimal learning stage, where more training produces modest progress and avoids overfitting, when the MSE curve flattens. This behavior confirms that the ANN model is stable, well-trained, and appropriate for precisely predicting the physical responses of the system.

$$Cf(\mathrm{Re}_x^{1/2}) = -0.7375 + 0.3760L_1 - 0.6675L_2 - 0.2921Nt - 0.0946L_1^{\,2} - 0.000L_2^{\,2} + 0.0701Nt^2 - 0.6528L_1L_2 + 0.4314L_1Nt + 0.1814L_2Nt \quad (28)$$

$$Nu(\mathrm{Re}_x^{-1/2}) = 0.1460 - 1.5295L_1 - 0.6467L_2 + 0.1764Nt + 0.6597L_1^{\,2} + 0.7562L_2^{\,2} + 0.2277Nt^2 + 0.2937L_1L_2 + 0.7270L_1Nt + 0.6026L_2Nt \quad (29)$$

$$\frac{\partial\left(Cf(\mathrm{Re}_x^{1/2})\right)}{\partial L_1} = 0.3760 - 0.1892L_1 - 0.6528L_2 + 0.4314Nt \quad (30)$$

$$\frac{\partial\left(Cf(\mathrm{Re}_x^{1/2})\right)}{\partial L_2} = -0.6675 - 0.0008L_2 - 0.6528L_1 + 0.1814Nt \quad (31)$$

$$\frac{\partial\left(Cf(\mathrm{Re}_x^{1/2})\right)}{\partial Nt} = -0.2921 + 0.1402Nt + 0.4314L_1 + 0.181L_2 \quad (32)$$

$$\frac{\partial\left(Nu(\mathrm{Re}_x^{-1/2})\right)}{\partial L_1} = -1.5295 + 1.3194L_1 + 0.2937L_2 + 0.7270Nt \quad (33)$$

$$\frac{\partial\left(Nu(\mathrm{Re}_x^{-1/2})\right)}{\partial L_2} = -0.6467 + 1.5124L_2 + 0.2937L_1 + 0.6026Nt \quad (34)$$

$$\frac{\partial\left(Nu(\mathrm{Re}_x^{-1/2})\right)}{\partial Nt} = 0.1764 + 0.4554Nt + 0.7270L_1 + 0.6026L_2 \quad (35)$$

Table 6. Sensitivity Analysis of the Skin friction Coefficient at $L_1 = 0$

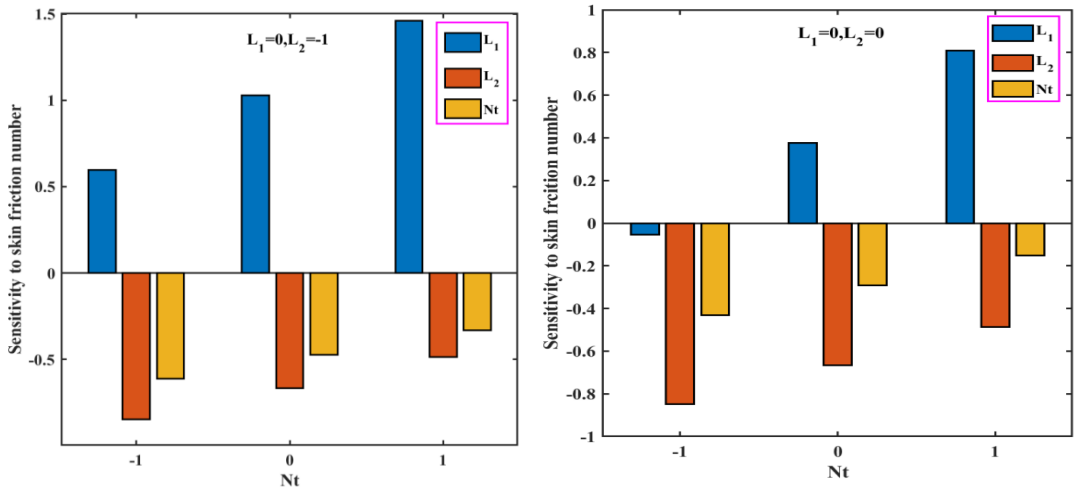
L_1	L_2	Nt	$\frac{\partial\left(C_f \mathrm{Re}x^{1/2}\right)}{\partial L_1}$	$\frac{\partial\left(C_f \mathrm{Re}x^{1/2}\right)}{\partial L_2}$	$\frac{\partial\left(C_f \mathrm{Re}x^{1/2}\right)}{\partial Nt}$
0	-1	-1	0.5974	-0.8481	-0.6123
0	-1	0	1.0288	-0.6667	-0.4721
0	-1	1	1.4602	-0.4853	-0.3319
0	0	-1	-0.0554	-0.8489	-0.4323
0	0	0	0.3760	-0.6675	-0.2921
0	0	1	0.8074	-0.4861	-0.1519
0	1	-1	-0.7082	-0.8497	-0.2523
0	1	0	-0.2768	-0.6683	-0.1121
0	1	1	0.1546	-0.4869	0.0281

The sensitivity indices of the response function related to the skin friction coefficient under different combinations of the velocity slip parameter, energy slip parameter, and thermophoresis parameter are shown in Table 6. The table illustrates how each parameter affects near-wall momentum transmission individually as well as through their coupled interactions. Improving the design and functionality of sophisticated thermal-fluid systems requires determining the factors that have the biggest impact on surface friction.

Table 7. Sensitivity Analysis of the Nusselt Number Coefficient at $L_1 = 0$

L_1	L_2	Nt	$\frac{\partial\left(Nu\,\mathrm{Re}\,x^{-1/2}\right)}{\partial L_1}$	$\frac{\partial\left(Nu\,\mathrm{Re}\,x^{-1/2}\right)}{\partial L_2}$	$\frac{\partial\left(Nu\,\mathrm{Re}\,x^{-1/2}\right)}{\partial Nt}$
0	-1	-1	-2.5502	-2.7617	-0.8816
0	-1	0	-1.8232	-2.1591	-0.4262
0	-1	1	-1.0962	-1.5565	0.0292
0	0	-1	-2.2565	-1.2493	-0.2790
0	0	0	-1.5295	-0.6467	0.1764
0	0	1	-0.8025	-0.0441	0.6318
0	1	-1	-1.9628	0.2631	0.3236
0	1	0	-1.2358	0.8657	0.7790
0	1	1	-0.5088	1.4683	1.2344

The sensitivity analysis of the Nusselt number for the same set of parameters is shown in Table 7. It demonstrates how the combined impact of these factors influences the rate of heat transmission, demonstrating that convective heat transfer is greatly enhanced by both radiation and magnetic effects. When constructing or modifying nanofluid-based thermal systems to achieve the necessary heat-transfer performance, the quantitative results aid in identifying the important factors that should be prioritized. All things considered, Tables 6 and 7 provide crucial direction by identifying the most significant factors, which is necessary for efficient system optimization and control.



(a) (b)

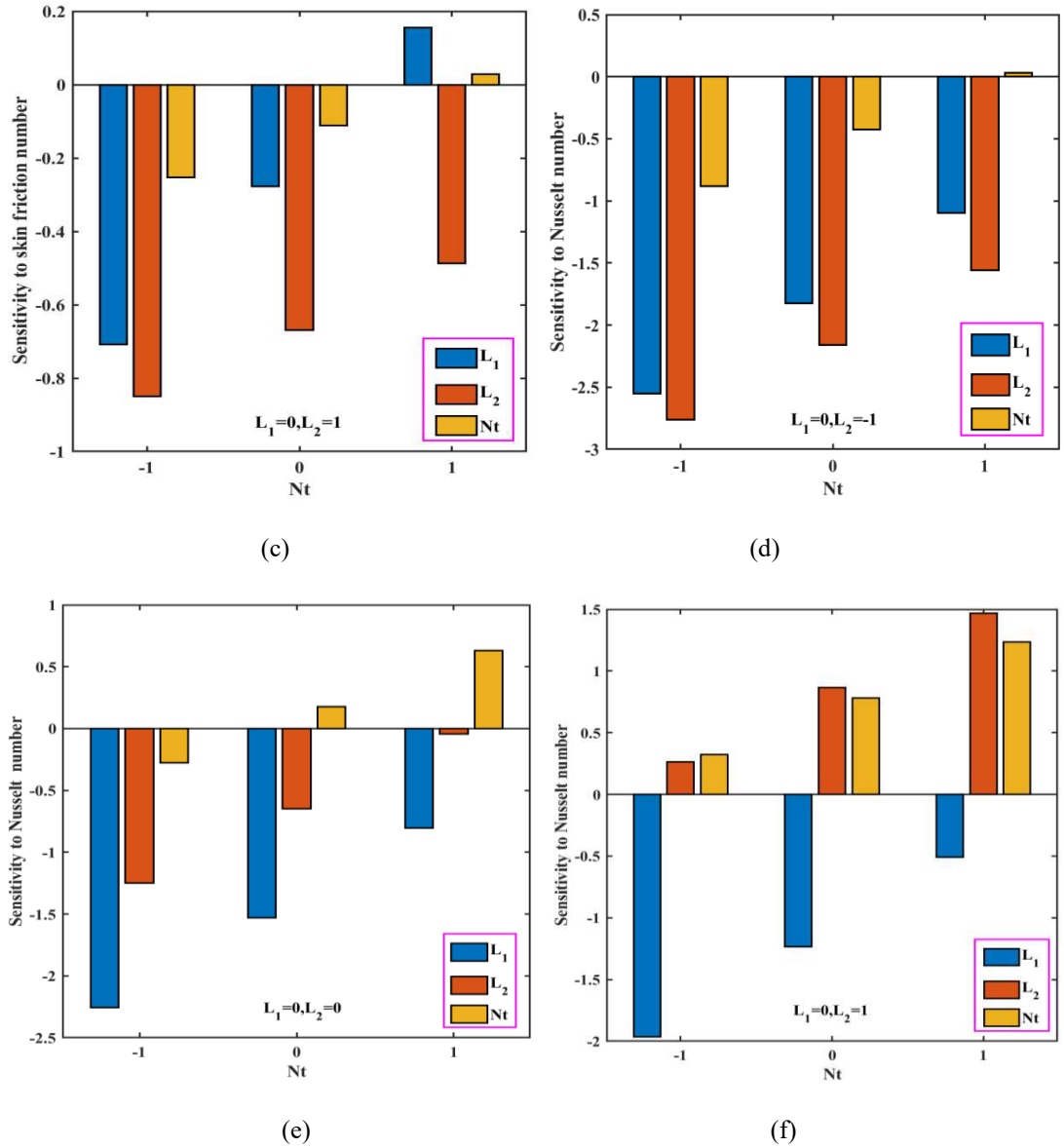


Fig. 28 Sensitivity analysis plots for (a-c) skin friction and (d-f) Nusselt number

The sensitivity analysis of the output responses skin friction (a–c) and Nusselt number (d–f) regarding the important slip and thermophoretic parameters, specifically L_1 (velocity slip), L_2 (energy slip), and Nt (thermophoresis parameter), is shown in Figure 28. The physical mechanisms and relative dominance of each controlling parameter are highlighted by the influence of the trends. By weakening the no-slip restriction at the wall, an increase in the velocity slip parameter L_1 lowers shear stress and, consequently, skin friction. Each controlling parameter's relative dominance and physical mechanisms are highlighted by the influence of trends. The no-slip restriction at the wall is weakened by an increase in the velocity slip parameter L_1, which lowers shear stress and, consequently, skin friction. Heat transport is also impacted by this decrease in wall-fluid interaction, which causes a slight drop in the Nusselt number. In a similar vein, raising the energy slip parameter L_2 lowers the heat flux at the surface by reducing the thermal coupling between the fluid and the wall. Both the skin friction (because to reduced momentum diffusion) and the Nusselt number (because of suppressed temperature gradients) are decreased by this weaker thermal exchange. The thermophoresis parameter Nt, on the other hand, exhibits a larger positive sensitivity on thermal transport because its amplification modifies the effective thermal boundary layer by increasing particle migration away from hotter locations.

Table 8. Minimization Strategy for the Skin-Friction Coefficient (Cf)

L_1	L_2	Nt	C_f	Nu	Desirability
0.6009	0.2463	0.0230	-0.519	0.2894	1.000

Table 9. Maximization strategy for the Nusselt Number Coefficient (Nu)

L_1	L_2	Nt	C_f	Nu	Desirability
0.6003	0.2617	0.0314	-0.520	0.3158	1.000

The optimal parameter choices for lowering skin friction and raising the Nusselt number are summarized in Tables 8 and 9 using the desirability-based multi-objective optimization method. The best combination found is $L_1 = 0.6009$, $L_2 = 0.2463$, and Nt = 0.0230. The model forecasts the highest heat-transfer rate (Nu = 0.2894), the lowest skin friction (Cf = −0.519), and an overall desirability of 1.000 at these values. Table 9 reports a higher Nusselt number (Nu = 0.3158) with a desire value of 1.000 under the identical conditions. These findings demonstrate that high thermal transfer and low drag can be successfully balanced under a single operating environment. This parameter offers the optimum balance between the two goals, as confirmed by the outstanding desirability score. The practical design of energy-storage/heat-extraction systems, improved fluid-flow technologies, and thermal management devices can all benefit from this ideal zone.

4.2 Conclusion:

The paper addresses the magnetohydrodynamic nanofluid flow over a radiatively heated vertical sheet, where the key parameters are optimized and assessed by analytical and numerical techniques. The effects of velocity slip, energy slip and thermophoresis on heat and mass transfer characteristics are discussed in detail, and the main conclusions are summarized as follows: This study applies Response Surface Methodology (RSM) to the problem of predicting the outcomes of slip flow across a vertical sheet. To comprehend their functions in the transport of momentum, heat, and mass, the parametric effects of thermal slip, thermophoresis, and velocity slip are examined.

- The near-wall velocity is improved while the velocity farther from the sheet is reduced when the value goes from 0.7 to 1.1. While the Nusselt number drops 2.78% points, the dipole profile goes up, which causes skin friction to go up 28% points.
- A decrease of 3.3% in skin friction and a decrease of 19.3% in the Nusselt number, signifying reduced heat transport, are produced by increasing the thermal slip parameter L_2 from 0.3 to 0.7, which in turn reduces the temperature, concentration, and solutal concentration profiles.
- The temperature, dipole, concentration, and solutal concentration profiles are elevated from 0.01 to 0.05, resulting in a 0.2% drop in skin friction and a 2.8% drop in the Nusselt number.

4.3 Future work:

The present work provides a basis for understanding the effects of velocity slip, energy slip and thermophoresis on the nanofluid heat and mass transfer. However, several aspects are still open to future investigation. Firstly, the present analysis is restricted to steady two-dimensional laminar flow with constant physical properties, while real systems often exhibit unsteady behaviour, turbulence and spatial variations. Future work therefore should extend the model to unsteady, turbulent and fully three-dimensional configurations including complex geometries and varying thermal boundary conditions. Further, consideration of non-uniform nanoparticle dispersion and higher particle loadings will help to more accurately depict practical industrial and biomedical applications. The combination of predictive techniques with machine learning and optimization strategies can further enhance the model accuracy and applicability, thus enabling better thermal management performance in advanced engineering systems.

Author contributions statement
S Ramesh contributed to conceptualization, methodology, investigation, designing, analyzed, data interpretation, and drafting the manuscript. H Niranjan contributed to important intellectual content, Investigation, supervision, reviewing, and editing. All authors reviewed the manuscript.

Acknowledgments
The authors are grateful to the anonymous referee for their helpful comments and valuable.
suggestions, which led to the improvement of the manuscript.

Declaration of competing interest
The authors declare that they have no known competing financial interests or personal relationships that could have appeared to influence the work reported in this paper.

Funding
This work received no external funding.

Data availability
The datasets generated and analysed during the current study are available from the corresponding author on reasonable request.

References

1. Felicita, A., Venkatesh, P., Gireesha, B. J. & Krishnamurthy, M. R. Slip and convective flow of Williamson nanofluid influenced by Brownian motion and thermophoresis mechanism in a horizontal microchannel. *Proc. Inst. Mech. Eng. Part N J. Nanomater. Nanoeng. Nanosyst.* 239, 59–69 (2025). https://doi.org/10.1177/23977914231177340
2. Abbas, W., Megahed, A. M., Emam, M. S. & Sadek, H. M. MHD dissipative Powell–Eyring fluid flow due to a stretching sheet with convective boundary conditions and slip velocity. *Sci. Rep.* 13, 15674 (2023). https://doi.org/10.1038/s41598-023-42774-6
3. Algehyne, E. A., Alharbi, A. F., Saeed, A., Dawar, A., Kumam, P. & Galal, A. M. Numerical analysis of the chemically reactive EMHD flow of a nanofluid past a bi-directional Riga plate influenced by velocity slips and convective boundary conditions. *Sci. Rep.* 12, 15849 (2022). https://doi.org/10.1038/s41598-022-20050-3
4. Nayak, M. K., Shaw, S., Pandey, V. S. & Chamkha, A. J. Combined effects of slip and convective boundary condition on MHD 3D stretched flow of nanofluid through porous media inspired by non-linear thermal radiation. *Indian J. Phys.* 92, 1017–1028 (2018). https://doi.org/10.1007/s12648-017-1158-6.
5. Ali, A., Khan, H. S., Saleem, S. & Hussan, M. EMHD nanofluid flow with radiation and variable heat flux effects along a slandering stretching sheet. *Nanomaterials* 12, 3872 (2022). https://doi.org/10.3390/nano12213872.
6. Ayub, M., Abbas, T. & Bhatti, M. M. Inspiration of slip effects on electro magneto hydrodynamics (EMHD) nanofluid flow through a horizontal Riga plate. *Eur. Phys. J. Plus* **131**, 193 (2016). https://doi.org/10.1140/epjp/i2016-16193-3
7. Atif, S. M., Abbas, M., Rashid, U. & Emadifar, H. Stagnation point flow of EMHD micropolar nanofluid with mixed convection and slip boundary. *Complexity* **2021**, 3754922 (2021). https://doi.org/10.1155/2021/3754922
8. Afzal, M., Zahid, F., Alam, B. E., Jaradat, M. M., Siddique, I., Ali, B. & Ma, B. Investigating the behaviour of electro-magneto-hydrodynamic Carreau nanofluid flow with slip effects over a stretching cylinder. *Nanotechnol. Rev.* **14**, 20250166 (2025). https://doi.org/10.1515/ntrev-2025-0166
9. Kumar, E. R., Reddy, N. N., Amar, N., Goud, B. S. & Srinivasulu, T. Analysis of slippery EMHD nano flow over a chemically reactive, stretchable porous sheet with a non-uniform heat source for developing novel applications. *Prog. Eng. Sci.* **2**, 100099 (2025). https://doi.org/10.1016/j.pes.2025.100099
10. Mkhatshwa, M. P. & Khumalo, M. Irreversibility scrutinization on EMHD Darcy–Forchheimer slip flow of Carreau hybrid nanofluid through a stretchable surface in porous medium with

temperature-variant properties. *Heat Transfer* **52**, 395–429 (2023). https://doi.org/10.1002/htj.22700
11. Kundu, B. & Saha, S. Review and analysis of electro-magnetohydrodynamic flow and heat transport in microchannels. *Energies* **15**, 7017 (2022). https://doi.org/10.3390/en15197017
12. Sharma, B. K., Kumar, A., Gandhi, R., Bhatti, M. M. & Mishra, N. K. Entropy generation and thermal radiation analysis of EMHD Jeffrey nanofluid flow: Applications in solar energy. *Nanomaterials* **13**, 544 (2023). https://doi.org/10.3390/nano13030544
13. Sarma, N. & Paul, A. Thermophoresis and Brownian motion influenced bioconvective cylindrical shaped Ag–CuO/H_2O Ellis hybrid nanofluid flow along a radiative stretched tube with inclined magnetic field. *BioNanoScience* **14**, 1266–1292 (2024). https://doi.org/10.1007/s12668-023-01280-1
14. Thumma, T., Mishra, S. R., Pattnaik, P. K. & Reddy, C. A. Exploring MHD radiative Maxwell nanofluid flow on an expanding surface for the impact of activation energy associated with velocity slip and convective boundary conditions. *J. Therm. Anal. Calorim.* **150**, 3661–3681 (2025). https://doi.org/10.1007/s10973-024-13905-y
15. Sivanandam, S. & Alqurashi, T. J. Activation energy and cross-diffusion effects on 3D rotating nanofluid flow in a Darcy–Forchheimer porous medium with radiation and convective heating. *Open Phys.* **23**, 20250186 (2025). https://doi.org/10.1515/phys-2025-0186
16. Yasmin, H., Bossly, R., Alduais, F. S., Al-Bossly, A. & Saeed, A. Heat transfer enhancement in magnetohydrodynamic hybrid nanofluids over a bi-directional extending sheet with slip and convective conditions. *Case Stud. Therm. Eng.* **63**, 105396 (2024). https://doi.org/10.1016/j.csite.2024.105396
17. Das, K. Slip effects on MHD mixed convection stagnation point flow of a micropolar fluid towards a shrinking vertical sheet. *Comput. Math. Appl.* **63**, 255–267 (2012). https://doi.org/10.1016/j.camwa.2011.11.018
18. Bilal, M. Micropolar flow of EMHD nanofluid with nonlinear thermal radiation and slip effects. *Alex. Eng. J.* **59**, 965–976 (2020). https://doi.org/10.1016/j.aej.2020.03.023
19. Yasmin, H. Numerical investigation of heat and mass transfer study on MHD rotatory hybrid nanofluid flow over a stretching sheet with gyrotactic microorganisms. *Ain Shams Eng. J.* **15**, 102918 (2024). https://doi.org/10.1016/j.asej.2024.102918
20. Gautam, A. K., Rajput, S., Bhattacharyya, K., Pandey, A. K., Chamkha, A. J. & Begum, M. Comparative study of two non-Newtonian fluids with bioconvective induced MHD flow in presence of multiple slips, heat source/sink and nonlinear thermal radiation. *Chem. Eng. J. Adv.* **12**, 100365 (2022). https://doi.org/10.1016/j.ceja.2022.100365
21. Rammoorthi, R. & Mohanavel, D. Entropy generation and sensitivity analysis for a squeezed flow of a Williamson hybrid nanofluid under the supervision of microcantilever sensor. *Results Eng.* **24**, 103464 (2024). https://doi.org/10.1016/j.rineng.2024.103464
22. Mustafa, M., Khan, J. A., Hayat, T. & Alsaedi, A. Buoyancy effects on the MHD nanofluid flow past a vertical surface with chemical reaction and activation energy. *Int. J. Heat Mass Transf.* **108**, 1340–1346 (2017). https://doi.org/10.1016/j.ijheatmasstransfer.2017.01.029
23. Devi, G. L., Niranjan, H. & Sivasankaran, S. Effects of chemical reactions, radiation, and activation energy on MHD buoyancy induced nanofluid flow past a vertical surface. *Sci. Iran.* **29**, 90–100 (2022). https://doi.org/10.24200/sci.2021.56835.4934
24. Islam, S., Ali, M. Y. & Reza-E-Rabbi, S. Comparative simulation of nonlinear radiative nano Casson and Maxwell fluids with periodic magnetic force and sensitivity analysis. *Heliyon* **10**, e29306 (2024). https://doi.org/10.1016/j.heliyon.2024.e29306
25. Balamurugan, R. & Vanav Kumar, A. Mixed convection of transient MHD stagnation point flow over a stretching sheet with quadratic convection and thermal radiation. *Heat Transfer* **53**, 584–609 (2024). https://doi.org/10.1002/htj.22965
26. Panda, S., Ontela, S., Pattnaik, P. K. & Mishra, S. R. Optimizing heat transfer rate with sensitivity analysis on nonlinear radiative hydromagnetic hybrid nanofluid flow considering catalytic effects and slip condition: Hamilton–Crosser and Yamada–Ota modelling. *Z. Angew. Math. Mech.* **104**, e202301064 (2024). https://doi.org/10.1002/zamm.202301064
27. Pei, Y., Liu, Q., Wang, C. & Wang, G. Energy efficiency prediction model and energy characteristics of subsea disc pump based on velocity slip and similarity theory. *Energy* **229**, 120690 (2021). https://doi.org/10.1016/j.energy.2021.120690
28. Aruna, J. & Niranjan, H. An artificial neural network approach to comparative aspects: A predictive analysis of magnetic dipole on the heat transfer of Maxwell hybrid nano coolants flow in an inclined cylinder. *Case Stud. Therm. Eng.* **68**, 105825 (2025). https://doi.org/10.1016/j.csite.2025.105825

29. Kotnurkar, A. S. & Mali, G. Influence of induced magnetic field and surface roughness of Casson nanofluid flow over an exponentially stretching sheet. *J. Umm Al-Qura Univ. Appl. Sci.* **9**, 572–590 (2023). https://doi.org/10.1007/s43994-023-00068-z